PTEP

Prog. Theor. Exp. Phys. **2012**, 01A106 (33 pages)
DOI: 10.1093/ptep/pts006

Simulation of quantum chromodynamics on the lattice with exactly chiral lattice fermions

Sinya Aoki[1,2], Ting-Wai Chiu[3,4], Guido Cossu[5], Xu Feng[5], Hidenori Fukaya[6], Shoji Hashimoto[5,7,*], Tung-Han Hsieh[8], Takashi Kaneko[5,7], Hideo Matsufuru[5], Jun-Ichi Noaki[5], Tetsuya Onogi[6], Eigo Shintani[9], and Kouhei Takeda[5]

[1] *Graduate School of Pure and Applied Sciences, University of Tsukuba, Tsukuba, Ibaraki 305-8571, Japan*
[2] *Center for Computational Sciences, University of Tsukuba, Tsukuba, Ibaraki 305-8577, Japan*
[3] *Physics Department, National Taiwan University, Taipei 10617, Taiwan*
[4] *Center for Quantum Science and Engineering, National Taiwan University, Taipei 10617, Taiwan*
[5] *High Energy Accelerator Research Organization (KEK), Tsukuba, Ibaraki, 305-0801, Japan*
[6] *Department of Physics, Osaka University, Toyonaka, Osaka 560-0043, Japan*
[7] *School of High Energy Accelerator Science, The Graduate University for Advanced Studies (Sokendai), Tsukuba, Ibaraki 305-0801, Japan*
[8] *Research Center for Applied Sciences, Academia Sinica, Taipei 115, Taiwan*
[9] *RIKEN-BNL Research Center, Brookhaven National Laboratory, Upton, NY 11973, USA*
[*] E-mail: shoji.hashimoto@kek.jp

Received April 6, 2012; Accepted June 7, 2012; Published September 15, 2012

Numerical simulation of the low-energy dynamics of quarks and gluons is now feasible based on the fundamental theory of strong interaction, i.e. quantum chromodynamics (QCD). With QCD formulated on a 4D hypercubic lattice (called lattice QCD or LQCD), one can simulate the QCD vacuum and hadronic excitations on the vacuum using teraflop-scale supercomputers, which have become available in the last decade. A great deal of work has been done on this subject by many groups around the world; in this article we summarize the work done by the JLQCD and TWQCD collaborations since 2006. These collaborations employ Neuberger's overlap fermion formulation, which preserves the exact chiral and flavor symmetries on the lattice, unlike other lattice fermion formulations. Because of this beautiful property, numerical simulation of the formulation can address fundamental questions on the QCD vacuum, such as the microscopic structure of the quark–antiquark condensate in the chirally broken phase of QCD and its relation to SU(3) gauge field topology. Tests of the chiral effective theory, which is based on the assumption that the chiral symmetry is spontaneously broken in the QCD vacuum, can be performed, including the pion-loop effect test. For many other phenomenological applications, we adopt the all-to-all quark propagator technique, which allows us to compute various correlation functions without substantial extra cost. The benefit of this is not only that the statistical signal is improved but that disconnected quark-loop diagrams can be calculated. Using this method combined with the overlap fermion formulation, we study a wide range of physical quantities that are of both theoretical and phenomenological interest.

1. Introduction

Since the 1970s, quantum chromodynamics (QCD) has been understood as the fundamental theory of strong interaction, not just because it contains the necessary three internal degrees of freedom of quarks (called *color*) but because its scaling property at high energies (a few GeV or higher) precisely agrees with the experimental data, i.e. the asymptotic freedom. Since then, experimental data supporting QCD, including its quantum effects at high-loop orders, have been generated. These

experiments are essentially probing the perturbative aspects of QCD at high energy, while the non-perturbative dynamics at low energy (less than a GeV) still remains a theoretically difficult problem, and quantitative tests against experimental data are quite limited. The key properties of QCD at low energy are the confinement of quarks inside the hadrons and spontaneous chiral symmetry breaking in the QCD vacuum; the dynamics of hadrons reflects these fundamental properties. A solution for QCD must therefore reproduce these aspects if QCD is truly the fundamental theory of strong interaction at low energy scales too.

Solving QCD is difficult mainly because its vacuum is so complicated. There is no single dominant gauge field configuration (like the flat, perturbative vacuum in QED); it is not completely random either. There have been a lot of theoretical ideas for solving the QCD vacuum, including those based on the instanton, which is a classical solution of non-Abelian gauge theory, but without full success.

Lattice QCD is one of the methods for regularizing ultraviolet divergences and thus mathematically defining QCD [1]. One introduces a 4D hypercubic lattice and puts the physical degrees of freedom (the quark and gluon fields) on the lattice sites or on the links connecting two neighboring sites. The SU(3) gauge symmetry is preserved on the lattice, while the rotational and Lorentz invariances are manifestly violated. An important property of lattice QCD is that, unlike the commonly used dimensional regularization, whose definition involves perturbation theory, lattice regularization is well-defined in both the ultraviolet and infrared regimes. Since the regulated theory is mathematically well-defined, direct numerical calculation of the path integral through which the theory is quantized is possible, in principle. Thus, lattice QCD provides a theoretically valid method to perform a first-principles calculation of QCD, including its non-perturbative dynamics, at low energy.

The lattice QCD calculation requires huge computational resources, especially to incorporate the quark-loop effects in the path integral. Since the 1980s, lattice QCD has used the high-end supercomputers available at the time. It is remarkable that researchers of lattice QCD have even developed machines that lead the entire field of supercomputing. CP-PACS, developed by the University of Tsukuba, is one such example [2,3]. It won first place in the TOP500 supercomputer list in 1996.

The state of the art of lattice QCD simulations may be summarized as follows: *"Realistic simulation of QCD to study the static properties of hadrons is now feasible"*. This means that the inclusion of up, down, and strange sea quarks has become a standard at small enough lattice spacing ($a \lesssim 0.1$ fm) on large enough volume ($L \gtrsim 2.5$ fm) to hold a single hadron. The low-energy hadron spectrum, for instance, has been well reproduced by several lattice groups (for a recent review, see, for instance, [4]).

Although the recent progress in lattice QCD is impressive, it still has many limitations. One of these is the multi-scale problem. The scales that may enter in QCD phenomena span wide ranges: up and down quark masses ($\sim$5 MeV), the strange quark mass ($\sim$100 MeV), the QCD scale ($\sim$300 MeV), the charm quark mass ($\sim$1.5 GeV), and the bottom quark mass ($\sim$4.5 GeV). If one injects momenta into the system by electromagnetic probes, for instance, there are additional scales associated with them. Treating light quarks requires more computational cost that grows as $1/m_q^{2-3}$ with m_q the light quark mass; reducing the lattice spacing to treat heavy quarks needs more resources that typically scale as $1/a^7$ with a the lattice spacing. Therefore, a reasonable strategy for practical applications is to use "effective theories" such as the chiral perturbation theory (χPT) for light quarks and the heavy quark effective theory (HQET) for heavy quarks. The light and heavy quark masses for which these effective theories are valid have to be carefully investigated using lattice QCD calculations.

The main focus of this article is the spontaneously broken chiral symmetry in the QCD vacuum. In massless three-flavor QCD, there are $SU(3)_{\rm L} \otimes SU(3)_{\rm R} \otimes U(1)_V$ flavor symmetries ($U(1)_A$ is

violated by the axial anomaly), among which $SU(3)_{\rm L} \otimes SU(3)_{\rm R}$ is broken spontaneously down to $SU(3)_V$. Associated with this, pions, kaons, and η mesons become massless as Nambu–Goldstone (NG) bosons. (To be more precise, η is a mixture of an NG particle η_8 and a flavor-singlet pseudoscalar meson η_1 due to a finite non-negligible strange quark mass. The flavor-singlet meson stays massive after spontaneous chiral symmetry breaking.) The dynamics of these NG bosons is well described by the chiral effective theory [5], in which the energy scale of the massless NG modes is separated from other dynamical scales of QCD solely relying on the symmetry breaking pattern. The small perturbation from this low-energy limit can be systematically included in the effective theory, i.e. χPT [6], albeit with a large number of unknown parameters (low energy constants (LECs)). Using lattice QCD, it should be possible to reproduce these well-known (but not explained from QCD) phenomena and to determine the unknown parameters in χPT starting from the QCD Lagrangian.

Obviously, chiral symmetry plays a key role in describing the dynamics of spontaneous chiral symmetry breaking. On the other hand, there is a well-known problem in realizing chiral symmetry on the lattice. Namely, there is a mathematical theorem which states the non-existence of lattice fermion formulations that preserve both chiral and flavor symmetry at once (the Nielsen–Ninomiya theorem [7**?** ,8]), so that one has to choose a formulation which breaks either chiral (Wilson fermion) or flavor (staggered fermion) symmetry. Since such a key symmetry is violated on the lattice, the study of the phenomena relating to chiral symmetry breaking is rather obscured.

This unpleasant situation was drastically changed, at least in principle, by a new class of lattice fermions that preserve exact chiral symmetry without spoiling flavor symmetries, i.e. the domain-wall [9–11] and overlap [12,13] fermions. The key observation is that they satisfy a modified chiral symmetry, which is different from the continuum one by an amount that vanishes in the continuum limit [14]. In this way, the Nielsen–Ninomiya theorem can be avoided, and one can investigate spontaneous chiral symmetry breaking on the lattice starting with the manifestly chirally symmetric lattice action.

The JLQCD and TWQCD collaborations employed the overlap fermion to simulate dynamical quarks in 2- and $2+1$-flavor QCD. (Here, 2-flavor QCD stands for the system with up and down quarks in the sea; $2+1$-flavor QCD contains relatively heavy strange quarks in addition.) Although the numerical cost required to simulate QCD with the overlap fermion is much higher compared to other traditional fermion formulations (Wilson or staggered), simulations on reasonably large lattices can be made possible by applying recent theoretical and algorithmic improvements.

In this article we review the work done using this setup. In Sect. 2, the overlap fermion formulation is described in some detail. In particular, the relation to the topological charge of the SU(3) gauge field is emphasized. In order to make the overlap fermion simulation practically feasible, we introduce a scheme to fix the global topological charge of the lattice. The relevance and irrelevance of this simulation scheme is also explained. Sect. 3 describes the implementation of the overlap fermion in numerical simulations. The all-to-all quark propagator technique is also introduced. In Sect. 4 we discuss chiral symmetry breaking. Here, the Banks–Casher relation [15] plays a crucial role in quantifying the existence and strength of symmetry breaking. More detailed analysis on its finite volume and finite quark mass scaling can be done with the help of chiral effective theory applied on a finite volume. In Sect. 5 we summarize various physics outputs from the projects, including the analysis of pion and kaon masses and decay constants, pion and kaon form factors, neutral kaon mixing, extraction of physical quantities from $VV-AA$ vacuum polarization, $\pi^0 \to \gamma\gamma$ decay amplitude, and the nucleon sigma term and strange quark content. The simulation has also been used to determine the strong coupling constant through the perturbative expansion of the vacuum polarization function at

high energies as discussed in Sect. 6. An extension to the study of finite temperature is discussed in Sect. 7. Finally, a summary and future prospects are given in Sect. 8.

2. Lattice fermion formulation with exact chiral symmetry

In this section we describe the lattice fermion formulation that preserves chiral symmetry and discuss its relation to the topology of the gauge field configuration.

2.1. *Overlap fermion formulation*

The massless overlap-Dirac operator $D_{\rm ov}(0)$ [12,13] is defined by

$$D_{\rm ov}(0) = m_0[1 + \gamma_5 {\rm sgn}(H_W(-m_0))] \tag{2.1}$$

with the hermitian Wilson–Dirac operator $H_W(-m_0) = \gamma_5 D_W(-m_0)$ and a matrix sign function sgn. Using the definition of the conventional Wilson–Dirac operator $D_W(-m_0)$ with a large negative mass term $-m_0$ of the cutoff order $1/a$, one can show that $D_{\rm ov}(0)$ in (2.1) approaches the continuum Dirac operator $\not{D}$ in the limit of small lattice spacing a.

The overlap-Dirac operator $D_{\rm ov}(0)$ satisfies the Ginsparg–Wilson relation [16]

$$D_{\rm ov}(0)\gamma_5 + \gamma_5 D_{\rm ov}(0) = \frac{1}{m_0} D_{\rm ov}(0)\gamma_5 D_{\rm ov}(0), \tag{2.2}$$

with which one can show that the fermionic lattice action $S_f = \sum_x \bar{\psi}_x D_{\rm ov}(0)\psi_x$ has a symmetry under the transformation [14]

$$\begin{cases} \delta\psi = \gamma_5 \left(1 - \dfrac{1}{2m_0} D_{\rm ov}(0)\right) \psi, \\ \delta\bar{\psi} = \bar{\psi} \left(1 - \dfrac{1}{2m_0} D_{\rm ov}(0)\right) \gamma_5. \end{cases} \tag{2.3}$$

This transformation coincides with the normal chiral transformation $\delta\psi = \gamma_5\psi$, $\delta\bar{\psi} = \bar{\psi}\gamma_5$ in the limit of vanishing lattice spacing. The Ward–Takahashi identities derived from this transformation have the same form as the continuum ones after taking account of an appropriate modification of the γ_5 matrix. It may thus be considered as the desired chiral symmetry in practical applications.

Once the quark mass m_q is introduced, the overlap-Dirac operator is modified as

$$D_{\rm ov}(m_q) = \left(1 - \frac{m_q}{2m_0}\right) D_{\rm ov}(0) + m_q. \tag{2.4}$$

This form guarantees that the discretization effect of $O(a)$ vanishes after a "field rotation" of the fermionic field in the observable. The leading discretization effect is thus of order a^2.

2.2. *Exact chiral symmetry and topological charge*

Because of the Ginsparg–Wilson relation (2.2) and the γ_5-hermiticity property $D_{\rm ov}^\dagger(0) = \gamma_5 D_{\rm ov}\gamma_5$, an eigenvalue $\lambda_{\rm ov}$ of $D_{\rm ov}(0)$ satisfies $\lambda_{\rm ov} + \lambda_{\rm ov}^* = \lambda_{\rm ov}\lambda_{\rm ov}^*/m_0$. Namely, the eigenvalues lie on a circle defined by $|1 - \lambda_{\rm ov}/m_0|^2 = 1$ on the complex plane. Furthermore, the eigenvalues always appear together with their complex conjugates except for the exact zero modes $\lambda_{\rm ov} = 0$ and the real modes $\lambda_{\rm ov} = 2m_0$. These zero modes are chiral, i.e. either right-handed $\gamma_5\psi_0 = +\psi_0$ or left-handed $\gamma_5\psi_0 = -\psi_0$.

In continuum QCD, zero modes of the Dirac operator $\not{D}(\{A\})$ reflect the topological structure of the background gauge field $\{A\}$ on which $\not{D}(\{A\})$ is defined. In fact, the Atiyah–Singer index theorem

tells us that the numbers of right-handed and left-handed zero modes, $n_{\rm R}$ and $n_{\rm L}$ respectively, are related to the topological charge Q of the background gauge field as $n_{\rm L} - n_{\rm R} = Q$.

On the lattice, the definition of the topological charge Q is not unique, but by defining the topological charge density q as $q = \frac{1}{2}{\rm tr}[\gamma_5 D_{\rm ov}(0)]$ on the lattice using the overlap-Dirac operator $D_{\rm ov}(0)$, one can write the index theorem $n_{\rm L} - n_{\rm R} = Q$ with a natural definition on the global topological charge $Q = \sum_x q_x$. As anticipated, the left-hand side, $n_{\rm L} - n_{\rm R}$, appears from the Jacobian under the chiral transformation (2.3), while the right-hand side, q, can be shown to correspond to the topological charge density

$$q = \frac{1}{32\pi^2}\epsilon_{\mu\nu\rho\sigma}{\rm tr}[F_{\mu\nu}F_{\rho\sigma}] \tag{2.5}$$

in the continuum limit. Namely, for a sufficiently smooth gauge configuration, the topological charge density defined through ${\rm tr}[\gamma_5 D_{\rm ov}(0)]$ reproduces the form $\epsilon_{\mu\nu\rho\sigma}{\rm tr}[F_{\mu\nu}F_{\rho\sigma}]$ up to order a^2 discretization effects [17]. The overlap-Dirac operator thus provides a proper definition of the topological charge on the lattice.

2.3. *Physics at fixed topological charge*

The ground state of QCD must be the θ vacuum, which is a superposition of "vacua" carrying different global topological charges, in order to ensure the cluster decomposition property of physical observables. This means that the lattice QCD simulation must efficiently sample different topological sectors to reproduce the QCD vacuum.

This requirement is, however, not always easy to meet. Most of the present unquenched lattice QCD simulations use the hybrid Monte Carlo algorithm [18] which is based on a continuous change of the gauge configuration according to a molecular-dynamics-type evolution equation. Since the topological charge only has integer values, transition from one topological charge sector to another necessarily encounters a discontinuity along the evolution, which is not easy to trace with the finite step size introduced to approximate the molecular-dynamics evolution. With the lattice fermion formulations that explicitly violate chiral symmetry, this problem manifests itself only near the continuum limit, where the discontinuity on the border of the topological sectors gradually emerges, which is indeed observed in numerical simulations [19,20]. With the overlap-Dirac operator, the problem of a hardly changing topological charge already exists at finite lattice spacings, and a method to treat it has been developed (called the reflection/refraction trick) [21,22], but was found to be extremely costly to apply to large-scale simulations.

In view of this situation, one promising approach, for lattice QCD in general and for dynamical overlap fermions in particular, is to fix the global topological charge Q during the hybrid Monte Carlo simulation and try to extract physics from there. This is not ridiculous, because it is known that the fixed Q effect is a finite volume effect which vanishes in the infinite volume limit. A theoretical basis for estimating the finite volume effect when one extracts the physics in the θ vacuum from that at fixed topology is proposed in [23], extending the work by Brower *et al.* [24]. In the following, we briefly review the formalism. Interestingly, using this method, we can extract the topological susceptibility, which measures the strength of the topological excitations, from a fixed topology simulation, as discussed in Sect. 4.3.

Consider the partition function in the θ vacuum defined by

$$Z(\theta) \equiv \langle\theta|\theta\rangle = \exp[-VE(\theta)], \tag{2.6}$$

with $E(\theta)$ the vacuum energy density. The partition function at a fixed topological charge Q is a Fourier transformation of $Z(\theta)$

$$Z_Q = \frac{1}{2\pi}\int_{-\pi}^{\pi} d\theta\, Z(\theta)\exp(i\theta Q) = \frac{1}{2\pi}\int_{-\pi}^{\pi} d\theta\, \exp(-VF(\theta)), \tag{2.7}$$

where $F(\theta) \equiv E(\theta) - i\theta Q/V$.

For a large enough volume, we can evaluate the θ integral in (2.7) by saddle point expansion. The key is the fact that $\theta = 0$ is the global minimum of the function $E(\theta)$, which follows from the exact inequality $Z(0) > Z(\theta)$ by Vafa and Witten [25]. Assuming analyticity of $E(\theta)$ near $\theta = 0$, we can expand $E(\theta)$ as $E(\theta) = \frac{\chi_t}{2}\theta^2 + O(\theta^4)$, where the topological susceptibility χ_t at $\theta = 0$ is defined by

$$\chi_t = \frac{\langle 0|Q^2|0\rangle}{V} = \left.\frac{d^2E(\theta)}{d\theta^2}\right|_{\theta=0}. \tag{2.8}$$

The saddle point θ_c is given by $\theta_c = i(Q/\chi_t V)(1 + O(\delta^2))$ with $\delta \equiv Q/(\chi_t V)$. Neglecting exponentially suppressed terms and expanding in powers of $1/V$, we obtain

$$Z_Q = \frac{1}{\sqrt{2\pi\chi_t V}}\exp\left[-\frac{Q^2}{2\chi_t V}\right]\left[1 - \frac{c_4}{8V\chi_t^2} + O\left(\frac{1}{V^2}, \delta^2\right)\right]. \tag{2.9}$$

This shows that, as long as $\delta \ll 1$ (equivalently, $Q \ll \chi_t V$), the distribution of Q becomes Gaussian.

This analysis implies that, for small values of Q or δ, the saddle point is close to $\theta = 0$, which guarantees that the physics at fixed topology with small values of Q is almost the same as that in the $\theta = 0$ vacuum up to higher order corrections in $1/V$. Thus any physical quantity at fixed topology can always be expressed in terms of physical quantities in the $\theta = 0$ vacuum plus $1/V$ correction terms, which are also physical quantities in the $\theta = 0$ vacuum. By expressing physical quantities at $\theta = 0$ in terms of those at fixed topology with a systematic 1/V expansion, we can derive a general formula to extract physics at the θ vacuum from fixed topology simulations.

Similarly, consider an arbitrary correlation function in the θ vacuum $G(\theta) = \langle\theta|O_1O_2\cdots O_n|\theta\rangle$. The corresponding correlation function at a fixed topological charge Q is given, for instance if G is CP-even, by

$$G_Q^{\text{even}} = G(0) + G^{(2)}(0)\frac{1}{2\chi_t V}\left[1 - \frac{Q^2}{\chi_t V} - \frac{c_4}{2\chi_t^2 V}\right] + O(V^{-2}), \tag{2.10}$$

where $G^{(2)}(0)$ stands for the second derivative of $G(\theta)$ with respect to θ.

The formula (2.10) provides an estimate of the finite size effect due to the fixed topological charge. The leading correction is of order $O(1/V)$. For a more quantitative estimate, one needs to evaluate $G^{(n)}(0)$, which is not possible in general. An exception is the pionic quantities for which χPT may be used. In χPT, one can see that the θ angle appears as a complex phase of the quark mass. The θ dependence of the pion mass should then be $m_\pi^2(\theta) = m_\pi^2(0)\cos(\theta/N_f)$ at the leading order. Beyond the leading order, an estimate is possible along the same lines, though some LECs are involved [26].

Even when such theoretical knowledge is not available, one can still fit the lattice data obtained at different Q to finally extract $G(0)$, in principle. For some physical quantities we are going to discuss in this article, we calculate them at two different Q in order to investigate their Q dependence. Except for pionic quantities, we expect that the fixed Q effect is sub-leading in general, since the θ dependence of any physical quantity can enter only through the quark mass $m_q e^{i\theta/N_f}$. The counting of $O(1/V)$ applies only for this quark mass dependence. In fact, in our calculations we found no significant Q dependence except for the pion mass and decay constant at the smallest quark masses.

An interesting application of the formula (2.10) is the one for a correlation function of flavor-singlet pseudoscalar densities. At a fixed topology, a constant piece remains at long distances, which can be used to extract topological susceptibility as discussed in Sect. 4.3.

3. Simulation strategy

This section is largely devoted to the technical aspects of the numerical simulations. Those readers who are not interested in these techniques might want to jump to Sect. 4, where physics discussions start.

More detailed descriptions may be found in [27–29].

3.1. Implementation of the overlap fermion

The overlap-Dirac operator $D_{\rm ov}(0)$ defined in (2.1) involves a matrix sign function sgn applied on the kernel operator $H_W(-m_0)$. In order to calculate the sign function exactly one has to calculate all eigenvalues and eigenvectors of $H_W(-m_0)$, which requires a numerical cost of $O(V^3)$ for a lattice of volume V and thus is clearly impractical. Instead, we use a combination of direct calculation of the eigenmodes and rational approximation, which is a standard choice for the implementation of the overlap-Dirac operator at present (see, for instance, [30]). Namely, we decompose the sign function as

$$\mathrm{sgn}(H_W(-m_0)) = \sum_{i=1}^{N_{\rm ev}} \mathrm{sgn}(\omega_i) u_i u_i^\dagger + \epsilon(H_W(-m_0))P_{\rm high}, \tag{3.1}$$

where $N_{\rm ev}$ is the number of the eigenvalues ω_i of $H_W(-m_0)$ below some threshold ($|\omega_i| < \omega_{\rm th}$) and u_i denotes the corresponding eigenvector. The function $\epsilon(x)$ is a rational approximation to $\mathrm{sgn}(x)$ written as

$$\epsilon(x) = x\left(p_0 + \sum_{l=1}^{N_{\rm pole}} \frac{p_l}{x^2+q_l}\right), \tag{3.2}$$

which is applied after projecting out the low-lying modes by a projection operator $P_{\rm high} = 1 - P_{\rm low}$ with $P_{\rm low} = \sum_{i=1}^{N_{\rm ev}} u_i u_i^\dagger$. The numerical coefficients p_l and q_l in (3.2) can be determined to achieve the best approximation for a given interval $|x| \in [x_{\rm min}, x_{\rm max}]$ according to the min–max criterion (the Zolotarev approximation). The lower limit $x_{\rm min}$ of the approximation is fixed to the threshold $\omega_{\rm th}$ and the upper limit is set slightly above the highest eigenvalue of $H_W(-m_0)$, which is rather stable over Monte Carlo history. The approximation of the sign function can be made exponentially better by increasing the number of the poles $N_{\rm pole}$ in (3.2). We control the precision of the sign function approximation to be better than 10^{-7} at every step of the simulation. The number of poles $N_{\rm pole}$ thus required is around 8 or 10.

The rational approximation (3.2) applied for $H_W(-m_0)$ requires $N_{\rm pole}$ inversions of the matrices $H_W(-m_0)^2 + q_l$. These inversions can be calculated at once using the multi-shift conjugate gradient (CG) algorithm, with which the numerical cost for obtaining $N_{\rm pole}$ is essentially the same as the single inversion with the smallest shift q_l. Overall, the computational cost of multiplying the overlap-Dirac operator is typically 100–1,000 times higher than that for the standard Wilson–Dirac operator. This is the cost for realizing the exact (or very precise, at the level of 10^{-7}) chiral symmetry on the lattice.

A further speed-up is possible by introducing the so-called 5D solver. This introduces a block matrix of 4D matrices in each entry, some of which include the kernel operator $H_W(-m_0)$. The 5D matrix is designed such that its inversion produces an inverse of 4D $D_{\rm ov}(m_q)$ [31–34]. In our

experience, this method is faster than the direct method for applying (3.2), which requires nested CG loops for an inversion of $D_{\rm ov}(m_q)$, by a factor of 5–8.

3.2. *Low-mode spectrum of H_W and topology fixing*

The rational approximation (3.2) of the sign function becomes more difficult as the range of the approximation $[x_{\rm min}, x_{\rm max}]$ is made wider, i.e. one needs larger $N_{\rm pole}$ to achieve the same precision. The setting of the threshold $\omega_{\rm th} = x_{\rm min}$ therefore has a direct impact on the numerical cost. We wish to raise $\omega_{\rm th}$ as much as possible, but the cost for calculating and subtracting the low-lying modes of $H_W(-m_0)$ below $\omega_{\rm th}$ becomes more significant then, if there are a number of such low-lying modes. The density of the low-lying modes is thus related to the numerical cost of simulating the overlap fermion.

The low-lying modes of $H_W(-m_0)$ could also be an obstacle for the definition of the overlap-Dirac operator. In the absence of such low modes, the locality of the overlap-Dirac operator is mathematically established [35], even though the sign function potentially produces a non-local contribution. In the typical gauge configurations corresponding to a lattice spacing around 0.1 fm, however, there is non-zero density of low modes observed. Then, the locality of the overlap-Dirac operator, which is a necessary fundamental property for any lattice Dirac operator, is a delicate and dynamical problem, i.e. one has to require that the low-lying eigenmodes are themselves localized [36–38]. We therefore want to avoid the low modes of $H_W(-m_0)$ as much as possible, though the locality is satisfied in our simulation setup [39].

In our work we introduce unphysical fermionic degrees of freedom that produce a factor

$$\frac{\det[H_W(-m_0)^2]}{\det[H_W(-m_0)^2 + \mu^2]} \tag{3.3}$$

in the path integral measure [40]. The numerator corresponds to two copies of Wilson fermions with a mass of cutoff order $-m_0$; the denominator represents bosonic degrees of freedom with a twisted mass term μ. The overall effect of (3.3) is to suppress the near-zero modes of $H_W(-m_0)$ while high modes above μ are essentially unaffected. In particular, the exact zero modes of $H_W(-m_0)$ are strictly prohibited. With this unphysical term the low modes are highly suppressed and the simulation of the overlap fermion is made numerically feasible.

An important side effect of (3.3) is that it freezes the global topological charge in the Monte Carlo history, since the topology change necessarily associates a change of sign of a near-zero mode of $H_W(-m_0)$, according to the usual argument of the spectral flow. We therefore have to take account of the effect of fixed topological charge on physical quantities. This is already described in Sect. 2.3.

3.3. *Simulation setup*

Numerical simulations by the JLQCD and TWQCD collaborations are performed for both 2- and $2+1$-flavor QCD.

Two-flavor runs are carried out on $16^3 \times 32$ lattices at a lattice spacing $a \simeq 0.12$ fm. Two quark flavors corresponding to up and down quarks are degenerate in mass and cover the range of $m_s/6$–m_s (m_s is the physical strange quark mass) with six independent runs. Simulations are mainly done in the trivial topological sector $Q = 0$, and Q dependence is tested at one of the sea quark masses ($\sim m_s/2$) with $Q = -2$ and -4.

More realistic $2+1$-flavor runs are carried out on $16^3 \times 48$ and $24^3 \times 48$ lattices at a lattice spacing $a \simeq 0.11$ fm. Degenerate up and down quarks are taken in the range $m_s/5$–m_s for five independent

runs; the strange quark mass is fixed at two values sandwiching the physical strange quark mass. Again, the main runs are in the $Q = 0$ sector except for a run with the lightest up and down quark mass for which we also took $Q = 1$. The larger volume simulations on the $24^3 \times 48$ lattice are carried out at the two lightest up and down quark masses, where the finite volume effect would be most significant.

In addition to these main runs, which are suitable for calculations of most physical quantities at zero temperature, we generated lattices in an unusual setup, i.e. in the ϵ-regime. The ϵ-regime is defined as a parameter region where the quark mass is taken at a very small value on a finite volume lattice, so that the Compton wavelength of the pion is made longer than the extent of the box. Pion dynamics in this setup can be analyzed using chiral perturbation theory, and a comparison with the lattice data may provide a new opportunity to determine some LECs. In such studies, the exact chiral symmetry realized by the overlap fermion plays a crucial role in greatly simplifying the theoretical analysis.

We carried out dedicated runs to generate lattices in this ϵ-regime. For both 2- and $2 + 1$-flavors we set the up and down quark mass around 3 MeV, which is even lower than their physical values, on a lattice of size $16^3 \times 32$ and $16^3 \times 48$, respectively. We refer to these lattices as ϵ-regime runs in the following.

3.4. Measurement techniques

As already mentioned, the overlap-Dirac operator has a property that its eigenvalues lie on a circle on the complex plane $(1 - \lambda_{\rm ov}/m_0)(1 - \lambda^*_{\rm ov}/m_0) = 1$. In the limit of vanishing lattice spacing or for the low-lying modes $|\lambda_{\rm ov}| \ll 1/a$, the eigenvalues become pure imaginary as in the continuum theory. Another continuum-like property of the overlap-Dirac operator is that the eigenvectors of the complex-paired eigenvalues are simply related by γ_5 as $u_{\lambda^*} = \gamma_5 u_\lambda$. As a result, the eigenvalue problem of the overlap-Dirac operator $D_{\rm ov}(0)$ can be reduced to that of the half-size matrix $(1 \pm \gamma_5) D_{\rm ov}(0)$ or that of the hermitian operator $\gamma_5 D_{\rm ov}(0)$.

On each gauge configuration to be used in the calculations of physical quantities, we solve this eigenvalue problem numerically to obtain the low-lying eigenvalues $\lambda^{(k)}_{\rm ov}$ and eigenvectors $u^{(k)}$ roughly up to m_s and to store them on disks. The number of eigenmodes stored are 100 or 160 for $16^3 \times 32$ and $24^3 \times 48$ lattices, respectively.

The use of these eigenmodes is two-fold. First, they can be used for the preconditioning of the Dirac operator in its inversion. By subtracting the low-lying mode contribution $D_{\rm ov}(0) P_{\rm low} = \sum_{k=1}^{N_e} \lambda^{(k)}_{\rm ov} u^{(k)}(x) u^{(k)\dagger}(y)$ from the Dirac operator $D_{\rm ov}(0)_{x,y}$, the minimum eigenvalue of the matrix to invert, $D_{\rm ov}(m_q)^\dagger D_{\rm ov}(m_q)$, is raised from m_q^2 to roughly m_s^2, and thus the inversion is significantly accelerated and is made m_q-independent. This benefits all physics calculations to be done on these gauge configurations.

The second use of these eigenmodes is for an improvement of the statistical signal of hadronic correlation functions. The hadronic correlation functions are constructed from the quark propagators $D_{\rm ov}(m_q)^{-1}$. Since the low-mode contribution to this quark propagator can be written as

$$(D_{\rm ov}(m_q)^{-1})_{\rm low}(x, y) = \sum_{k=1}^{N_e} \frac{u^{(k)}(x) u^{(k)\dagger}(y)}{m_q + \left(1 - \dfrac{m_q}{2m_0}\right) \lambda^{(k)}_{\rm ov}}, \tag{3.4}$$

its calculation at different source points y does not require extra computational cost, provided that the low modes are stored on the disks. We may therefore average the low-mode contribution to the

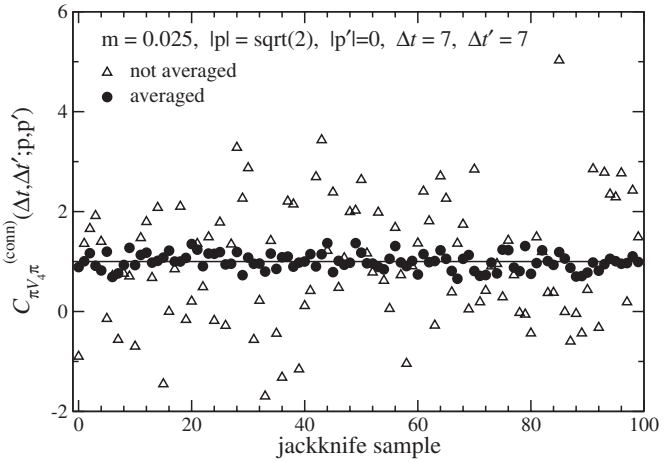

Fig. 1. Statistical fluctuation with (filled circles) and without (open triangles) the average over the source points. This is an example for a pion three-point function relevant to the pion electromagnetic form factor. Reproduced from [42].

hadronic correlation function over different source points with minimal additional cost. With this procedure one can substantially improve the statistical signal of the hadron correlation functions. It does not introduce any bias as far as the system has translational invariance.

The average over the source points can be extended beyond the low-lying modes by using a stochastic method. This is called the *all-to-all propagator* technique. In particular, we use its variant proposed in [41]. For a given gauge configuration, we prepare complex Z_2 or Z_4 noise vectors $\eta^{(d)}(x)$ with $d = 1, 2, \ldots N_d = 3 \times 4 \times N_t/2$, each of which has non-zero elements only for a single combination of color and spinor indices and at two consecutive time-slices. (This choice is made somewhat arbitrarily by taking account of its benefit and the computational cost.) The high-mode contribution is estimated as

$$(D_{\mathrm{ov}}(m_q)^{-1})_{\mathrm{high}}(x, y) = \sum_{d=1}^{N_d} x^{(d)}(x)\eta^{(d)\dagger}(y) \tag{3.5}$$

with the solution vector $x^{(d)}$ calculated by solving

$$\sum_y (D_{\mathrm{ov}}(m_q))(x, y)x^{(d)}(y) = \sum_y (\delta_{xy} - P_{\mathrm{low}}(x, y))\eta^{(d)}(y), \tag{3.6}$$

and stored on the disks. The computational cost is therefore proportional to N_d. Each inversion is accelerated by projecting out the low-mode contribution P_{low} as already mentioned. The estimate for the propagator $D_{\mathrm{ov}}(m_q)^{-1}$ is then given by adding the low-mode and high-mode contributions, $(D_{\mathrm{ov}}(m_q)^{-1})(x, y) = (D_{\mathrm{ov}}(m_q)^{-1})_{\mathrm{low}}(x, y) + (D_{\mathrm{ov}}(m_q)^{-1})_{\mathrm{high}}(x, y)$ for any sink and source points x and y, respectively.

With this all-to-all propagator, we may calculate, for instance, three-point functions for arbitrary choices of initial and final momenta without extra cost. The statistical signal is substantially improved, especially for pion correlation functions, as shown in Fig. 1. Calculation of the disconnected diagrams is another interesting application of this method, as discussed in the calculation of the strange quark content of the nucleon in Sect. 5.5.

4. Chiral symmetry breaking

In the following sections of this article we describe the physics results obtained from the dynamical overlap fermion simulations of QCD.

4.1. Chiral symmetry and lattice QCD

One of the fundamental properties of the QCD vacuum is the spontaneous breaking of chiral symmetry. Even before QCD, many important properties of low-energy hadrons, such as the GMOR relation and other soft pion theorems, were discovered based on the PCAC relation and current algebra. In the modern perspective, they are derived from the chiral effective theory, which is constructed assuming spontaneous chiral symmetry breaking. For theoretical understanding of the low-energy hadronic phenomena and the role played by strong interaction, therefore, a crucial step is to establish a link between QCD and chiral effective theory.

Chiral symmetry of course plays a key role in the understanding of chiral symmetry breaking. In the flavor non-singlet sector of chiral symmetry, pions arise as the Nambu–Goldstone (NG) boson associated with spontaneous symmetry breaking, while in the flavor-singlet sector the chiral symmetry is violated by the axial anomaly and is related to the topology of non-Abelian gauge theory. There are near-zero modes of quarks; their accumulation in the vacuum leads to symmetry breaking in the flavor non-singlet sector as indicated by the Banks–Casher relation [15]. These near-zero modes may also have a close relation to the topological excitations in QCD, because their cousins, exact zero modes, appear associated with topological excitations in QCD. In this way, the axial-anomaly in the flavor-singlet sector may be responsible for, or at least closely related to, the spontaneous chiral symmetry breaking in the flavor non-singlet sector. In order to study this complicated phenomenon on the lattice, it is important to preserve the chiral structure of the continuum fermion using the overlap fermion formulation.

The spontaneous chiral symmetry breaking is probed by the chiral condensate $\langle \bar{q}q \rangle$. Its lattice calculation requires special care because the scalar density operator $\bar{q}q$ has a power divergence of the form m_q/a^2 as the cutoff $1/a$ goes to infinity. The massless limit has to be taken to remove this large unphysical contribution and to obtain the physical result. (When the chiral symmetry is violated from the outset, as in Wilson-type fermions, the divergence is even stronger, $\sim 1/a^3$.) On the other hand, the chiral condensate must vanish in the massless limit, when the space-time volume is kept finite. Therefore, the proper order of the limits is to take the infinite volume limit first and then the massless limit, which is called the thermodynamical limit.

4.2. Spectral density and chiral condensate

The problem of the ultraviolet divergence can be avoided by focusing on the low-lying eigenmode spectrum of the Dirac operator. As indicated by the Banks–Casher relation [15], chiral symmetry breaking is induced by an accumulation of low-lying eigenmodes of the Dirac operator:

$$\lim_{m\to 0}\lim_{V\to\infty} \rho(\lambda = 0) = \frac{\Sigma}{\pi}, \tag{4.1}$$

where $\rho(\lambda)$ denotes the eigenvalue density of the Dirac operator defined by $\rho(\lambda) \equiv (1/V)\sum_k \langle \delta(\lambda - \lambda_k)\rangle$. The expectation value $\langle \cdots \rangle$ represents an ensemble average and k labels the eigenvalues of the Dirac operator on a given gauge field background. On the right-hand side of (4.1), Σ is the chiral condensate, $\Sigma = -\langle \bar{q}q \rangle$, evaluated in the massless quark limit. In the free theory, we expect a scaling $\rho(\lambda) \sim \lambda^3$ for dimensional reasons and thus $\rho(0) = 0$. The relation (4.1) implies that spontaneous

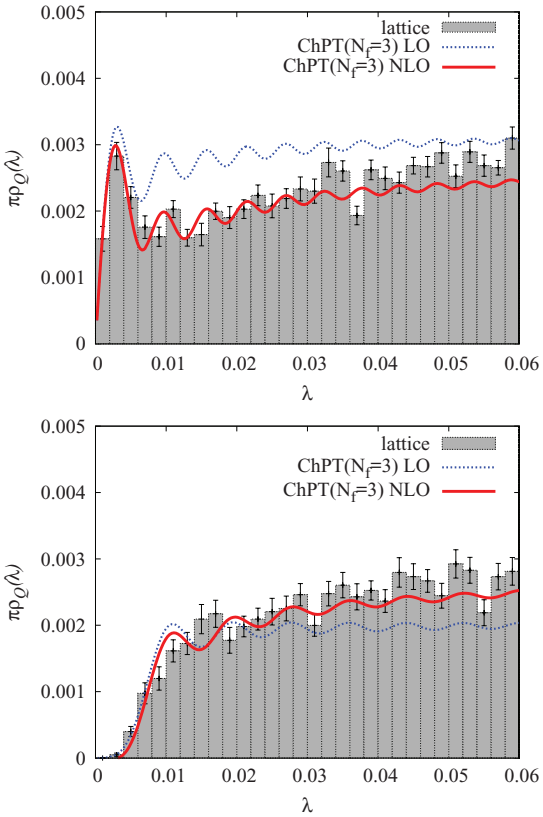

Fig. 2. Spectral density of the Dirac operator on the lattice (histogram) compared with the leading order (blue dots) and next-to-leading order χPT calculation (red curve) [43]. Top: the pion mass is around 300 MeV and the system is in the p-regime. Bottom: as above, for a small pion mass ($\sim$100 MeV). The system is in the ϵ-regime.

chiral symmetry breaking characterized by non-zero Σ is related to the number of near-zero modes in a given volume.

In practical work, taking the infinite volume and massless limit required in (4.1) is quite demanding. Instead, we use theoretical knowledge through χPT on the volume (V) and quark mass (m_q) scaling of $\rho(\lambda)$. Once we can check the scaling behavior with the lattice data taken at different values of V and m_q, we can safely extract the parameter Σ in the infinite volume limit. The most recent theoretical work [43] provides the V and m_q dependence of $\rho(\lambda)$ calculated to the one-loop level of χPT. This analytical calculation is valid in both the conventional p-regime and the nearly massless ϵ-regime.

Some of the results from [44–46] are shown in Fig. 2, which is obtained on the $2+1$-flavor lattice configurations at lattice spacing $\sim$0.11 fm and four-volume being $\sim (1.8\,\mathrm{fm})^3 \times (5.4\,\mathrm{fm})$. For the upper plot, the pion mass is around 300 MeV and the system is in the p-regime. (An earlier analysis in two-flavor QCD is found in [47,48].) The plot compares the result with the χPT calculation at the leading order (LO, blue dots) and the next-to-leading order (NLO, red curve) [43]. The leading order curve is the same as that obtained with the chiral random matrix theory, which depends only on a combination $m\Sigma V$ with the chiral condensate Σ, lattice volume V, and light quark mass m. In the oscillating curves each peak corresponds to a distribution of the first, second, third eigenvalue, and so on. The next-to-leading order formula involves the pion decay constant F and strange quark mass m_s as extra parameters.

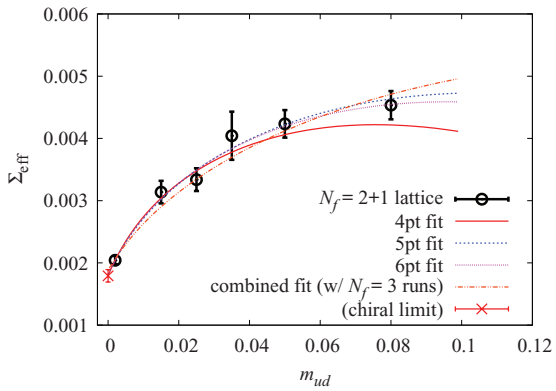

Fig. 3. Chiral extrapolation of the chiral condensate. Because of the data point in the ϵ-regime, the determination of the chiral limit is quite stable. Reproduced from [46].

We find that the shape of the spectrum is nicely reproduced by adding the next-to-leading order contribution, which reduces the height significantly from the second peak. The chiral condensate at a given quark mass is obtained by fitting this lattice data.

In the ϵ-regime, one expects that the lowest eigenvalues are suppressed by the fermion determinant $\prod_k(\lambda_k^2 + m^2)^2$, as m gets smaller than the lowest eigenvalue. This behavior is indeed realized on the ϵ-regime lattice as shown in Fig. 2 (bottom).

An extrapolation of the chiral condensate $\Sigma(m_{ud}, m_s)$ to the chiral limit of up and down quarks is shown in Fig. 3. The lattice data show a curvature, which is the pion-loop effect as predicted by χPT [6]:

$$\Sigma(m_{ud}, m_s) = \Sigma(0, m_s)\left[1 - \frac{3M_\pi^2}{32\pi^2F^2}\ln\frac{M_\pi^2}{\mu^2} + \frac{32L_6M_\pi^2}{F^2}\right]. \tag{4.2}$$

The data point close to the chiral limit, which is the ϵ-regime data, is helpful in identifying this curvature and for a stable chiral extrapolation. The result in the chiral limit of up and down quarks is

$$\Sigma^{\overline{\rm MS}}(0, m_s; 2\,{\rm GeV}) = [242(04)(^{+19}_{-18})\,{\rm MeV}]^3. \tag{4.3}$$

Conversion to the $\overline{\rm MS}$ scheme is performed with a non-perturbatively calculated renormalization constant through the RI/MOM scheme as an intermediate scheme [49].

Besides the spectral density, there are other ways to extract information on the QCD vacuum, for instance by calculating the meson correlation functions. In the p-regime this is standard practice, but by entering the ϵ-regime it makes it possible to determine the LECs avoiding the problems of chiral extrapolation. An attempt is made in [50], and the work is extended to the χPT analysis covering both p- and ϵ-regimes in a unified manner [51,52].

4.3. Topological susceptibility

The topological susceptibility $\chi_t = \langle Q^2\rangle/V$ measures the amount of topological excitations per unit volume. This quantity has an interesting relation to chiral symmetry breaking as suggested by the leading-order formula in χPT:

$$\chi_t = \frac{m\Sigma}{N_f}, \tag{4.4}$$

where m is the quark mass of N_f degenerate flavors [53]. Namely, there will be more topological excitations when there are more low-lying modes of Dirac operators accumulated in the vacuum.

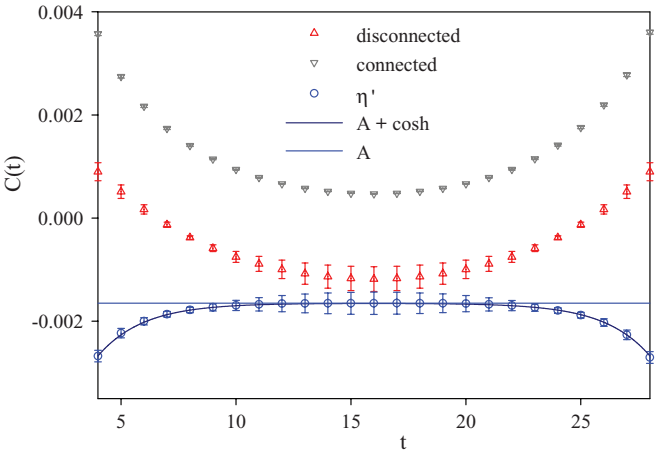

Fig. 4. Correlation function of the flavor-singlet pseudoscalar density operators calculated on a two-flavor lattice at a fixed topological charge $Q = 0$. Contributions from connected (lower triangles) and disconnected (upper triangles) diagrams are shown together with the total (blue circles). Reproduced from [54].

This non-trivial relation between topological excitation and chiral symmetry breaking is intriguing, since the index theorem relates the global topological charge to the number of exact zero modes, supporting the relation (4.4) at least qualitatively. One has to be careful though, because this mathematical theorem does not tell us anything about *near*-zero modes nor *local* topological excitations. For further dynamical questions, including the confirmation of (4.4), one has to use lattice QCD calculations.

In this subsection we describe the calculation of χ_t in our dynamical overlap fermion simulations. One might think that χ_t cannot be correctly calculated from the simulations with fixed topology, but it is indeed possible because χ_t is a measure of *local* topological excitations. At a fixed *global* topological charge, χ_t can be extracted from a long-range correlation of topological charge density operators using the formula (2.10) [23].

To be more explicit, we use the following formula, which is obtained by applying (2.10) to a correlation function of the flavor-singlet pseudoscalar densities $P(x)$,

$$\lim_{|x|\to\text{large}} \langle m P(x) m P(0)\rangle_Q = \frac{1}{V}\left(\frac{Q^2}{V} - \chi_t - \frac{c_4}{2\chi_t V}\right) + O(e^{-m_{\eta'}|x|}). \tag{4.5}$$

At a fixed topological charge Q, a constant piece remains after the physical excitation of the η' meson decays exponentially. From this constant term, we can extract the topological susceptibility χ_t.

A numerical example for two-flavor QCD is shown in Fig. 4, where the correlation function calculated on a $Q = 0$ sector is plotted. Since the flavor-singlet operators are involved, disconnected quark loop diagrams have to be evaluated in addition to the connected diagram, which is equivalent to the pion correlation function. The plot shows that, by subtracting the connected contribution from the disconnected one, the constant (negative) correlation can be identified. It is natural to have a negative correlation because the global topological charge Q is fixed to zero; when there is a positive (local) topological charge fluctuation found at a given lattice point, there will be more chance of finding a negative fluctuation apart from that location.

Near the chiral limit, χ_t is expected to behave as (4.4). For non-degenerate quark masses, m should be replaced by its inverse average, $(m_u^{-1} + m_d^{-1} + m_s^{-1})^{-1}$ for the case of $N_f = 3$. Our lattice results

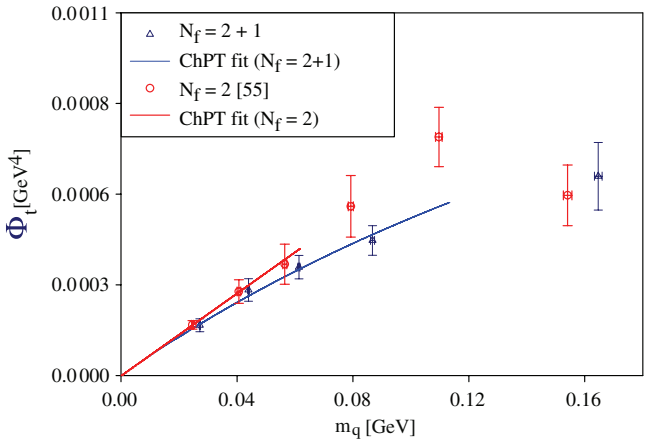

Fig. 5. Topological susceptibility χ_t as a function of sea quark mass. Lattice data are from [54,55].

[54–56] are shown in Fig. 5. The results from two-flavor and $2+1$-flavor QCD are well described by χPT. The chiral condensate Σ extracted from the slope of this plot is consistent with the one obtained from analysis of the spectral function. This means that topological excitations are indeed active in the QCD vacuum and their amount is just as expected from the chiral effective theory.

Through these studies, the spontaneous breaking of chiral symmetry is well established using the first-principles calculation of lattice QCD. The exact chiral symmetry provided by the overlap fermion plays a crucial role there. The χPT is confirmed to be valid near the chiral limit for fundamental quantities such as the chiral condensate and topological susceptibility.

One of the remaining questions is how much the region of χPT is extended towards wider applications and larger values of pion masses/momenta.

4.4. Convergence of chiral expansion

At Lattice 2002, the annual conference on lattice field theory, there was a panel discussion on the issue of chiral extrapolation of lattice data [57]. The problem at that time was that the curvature expected due to the chiral logarithm of the form $m_\pi^2 \ln m_\pi^2$ was not visible in lattice data even for pionic quantities, such as pion mass and decay constant. This was mainly because the quark mass in the dynamical fermion simulations at that time was too large (the pion mass was above 500 MeV), which is presumably out of the range of χPT. This led to a large systematic error in the chiral extrapolation.

Since then, by the development of algorithms and machines, the pion mass in the lattice simulations has been reduced to 200–300 MeV, and even physical point simulations are emerging. Note also that we even achieved a simulation in the ϵ-regime, where the quark mass is smaller than that of physical up and down quarks. It is therefore interesting to investigate the convergence property of the chiral expansion, using these available data.

The χPT provides a systematic expansion in terms of small m_π^2 and p^2, but the region of convergence of this chiral expansion is not known a priori. With the available one- and two-loop calculations of χPT we study the pion mass region, where the chiral expansion describes the lattice data well. With exact chiral symmetry, the test is conceptually clean, since no additional terms to describe the violation of chiral symmetry have to be introduced. (With other fermion formulations, this is not the case. For instance, staggered χPT is often used to analyze the lattice data obtained with the staggered

fermion. In many other cases where Wilson-type fermions are used, the correction terms are often simply ignored.)

For the pion mass m_π and decay constant f_π the chiral expansion is given as

$$\frac{m_\pi^2}{m_q} = 2B\left[1 + \frac{1}{2}x\ln x + c_3 x + O(x^2)\right], \tag{4.6}$$

$$f_\pi = f[1 - x\ln x + c_4 x + O(x^2)], \tag{4.7}$$

where m_π and f_π denote the quantities after the finite quark mass corrections while m and f are those at the leading order (the massless limit). The expansion parameter x in (4.6) and (4.7) could either be $x \equiv 2m^2/(4\pi f)^2$, $\hat{x} \equiv 2m_\pi^2/(4\pi f)^2$, or $\xi \equiv 2m_\pi^2/(4\pi f_\pi)^2$ (we use the notation of $f_\pi = 131$ MeV). They all give an equivalent description at this order, i.e. next-to-leading order (NLO), while the convergence behavior at higher orders may depend on the expansion parameter. The constants c_3 and c_4 are linear combinations of the LECs.

It is important to notice that the coefficients of the $x\ln x$ terms in (4.6) and (4.7) are determined only from the symmetry (flavor SU(2) in this case) and do not involve any free parameters. This prediction can be tested by analyzing the curvature in the x-dependence of m_π^2/m_q or f_π.

Figure 6 demonstrates the x dependence. It also shows a comparison of different expansion parameters, which are all equivalent at this order. The lattice data (black dots) are those in two-flavor QCD [58]. The lattice data in the region of small m_π^2 show a trend of the positive and negative curvature for m_π^2/m_q and f_π respectively, as expected from (4.6) and (4.7).

The curves in Fig. 6 are obtained by fitting the three lightest data points with the three expansion parameters, which provide equally precise descriptions of the data in the region of the fit. If we look at the heavier quark mass region, however, it is clear that only the ξ-expansion gives a reasonable function and others largely miss the data points. This clearly demonstrates that, at least for these quantities, the convergence of the chiral expansion is much better with the ξ-parameter than with the other conventional choices. This is understood as an effect of resummation of the chiral expansion by the use of the "renormalized" quantities m_π^2 and f_π. In fact, only with the ξ-expansion could we fit the data including the kaon mass region with the next-to-next-to-leading order (NNLO) formulae [58]. The results for $2+1$-flavor QCD are being analyzed [59–61].

With NLO formulae (like those in (4.6) or (4.7)), the convergence of the chiral expansion is marginal in the kaon mass regime. In fact, some groups decided not to use the SU(3) χPT for the kaon sector but use the SU(2) formula with the strange quark treated as a heavy particle. This corresponds to an expansion in terms of m_{ud}/m_s and is a theoretically consistent treatment, though the predictive power of χPT is lost to some extent.

5. Light hadron phenomenology

In this section we describe the physics results obtained for other phenomenologically interesting quantities. In many of these, the exact chiral symmetry of the overlap fermion formulation plays a unique role.

5.1. Pion form factor

The pion electromagnetic form factor $F_V(q^2)$ is defined by

$$\langle\pi(p')|V_\mu|\pi(p)\rangle = (p+p')_\mu F_V(q^2), \tag{5.1}$$

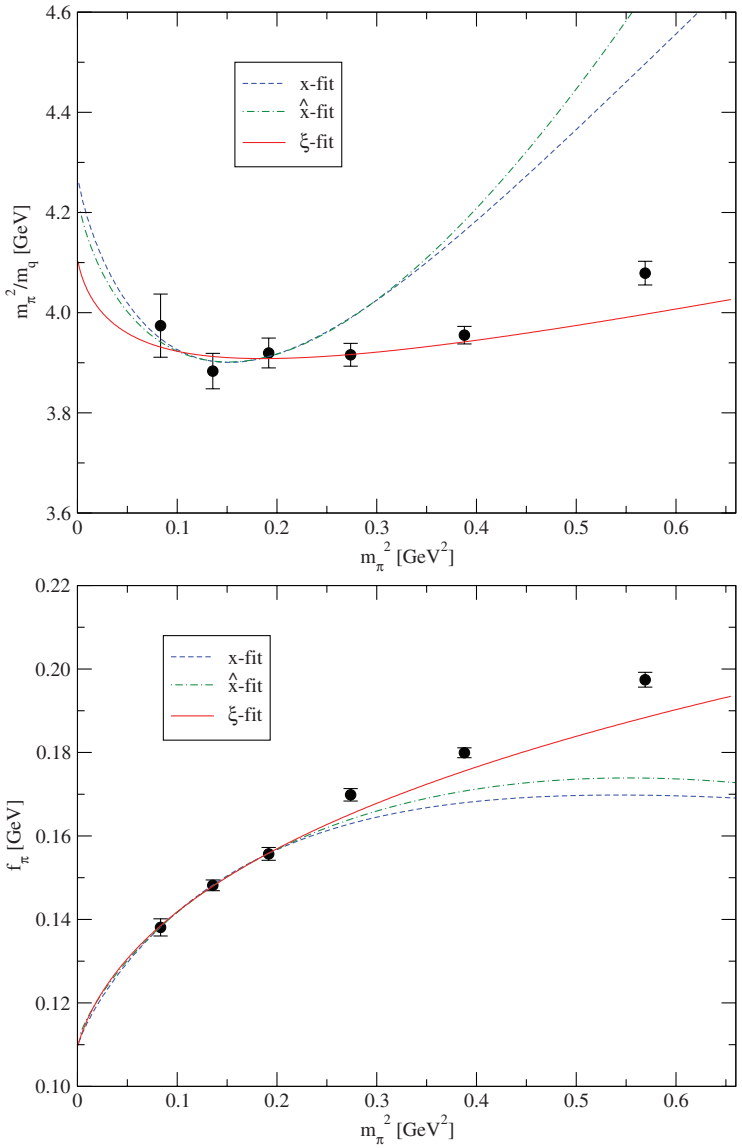

Fig. 6. Comparison of chiral expansion in terms of x, $\hat{x}$, and ξ. The plots represent m_π^2/m_q (top) and f_π (bottom). Fits of the three lightest data points with the NLO ChPT formulae (4.6) and (4.7) are shown with three choices of the expansion parameters x, $\hat{x}$, and ξ. (See the text for details.) The results are from [58].

for a momentum transfer $q_\mu = (p - p')_\mu$. V_μ represents a vector current made of quark fields. The electromagnetic charge radius of the pion is defined through this form factor as $\langle r^2 \rangle_V = 6(\partial F_V(q^2)/\partial q^2)_{q^2=0}$. Calculation of this form factor provides a good testing ground for the lattice calculations of more complicated form factors, as there exist precise experimental data. Calculations to two-loop precision are also available in the χPT framework, and can be compared with the lattice calculation.

The form factor can be obtained through a three-point function of the form $\langle P V_\mu P^\dagger \rangle$, with $P^{(\dagger)}$ an appropriate interpolating operator to efficiently produce or annihilate a pion state with a specific momentum. Using the all-to-all propagator technique discussed in Sect. 3.4, we can calculate the pion form factor with various initial and final state momenta without substantial extra computational cost. Figure 7 shows the lattice data at the lowest available pion mass (∼300 MeV) [42]. The

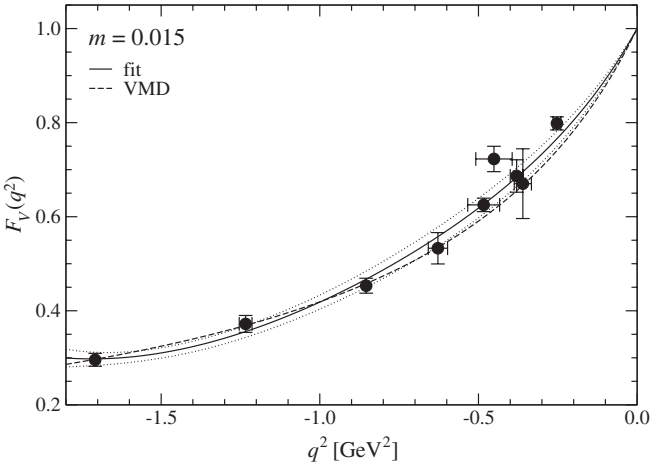

Fig. 7. Pion electromagnetic form factor calculated on the lattice at a pion mass around 300 MeV. The dashed line represents the vector meson dominance (VMD) ansatz, while the solid curve with an error band is our fit that includes correction terms by a polynomial expansion. Reproduced from [42].

data are fitted with various functional forms including the vector meson dominance (VMD) ansatz $F_V(q^2) = 1/(1 - q^2/M^2_{\rm pole})$ and its modifications, including the effects of higher resonances as shown in the plot.

The pion charge radius, which is extracted from the fit of the form factor, provides an interesting opportunity to test χPT, since it predicts a characteristic logarithmic divergence in the massless pion limit. Namely, at the next-to-leading order (NLO), the formula is given as

$$\langle r^2 \rangle = -\frac{1}{(4\pi F)^2}(1 + 6N l_6^r) - \frac{1}{(4\pi F)^2} \ln \frac{m_\pi^2}{\mu^2}. \tag{5.2}$$

Here F is the pion decay constant in the chiral limit and l_6^r is one of the LECs. Note that the coefficient of the log term is fixed and the pion mass dependence is entirely determined by the effective theory at this order.

A fit of our lattice data is shown in Fig. 8 (top). In the lattice data, we find the expected pion mass dependence going upward towards the chiral limit, but the value obtained after extrapolation to the physical pion mass is still significantly lower than the experimental data. We extend the analysis to include the next-to-next-to-leading order (NNLO) terms in χPT, for which the result is plotted in Fig. 8 (bottom). Curvature towards the chiral limit is more enhanced and the result is consistent with the experimental data.

For a more detailed description of the analysis we refer the reader to [42], but an important lesson from this analysis is that the NNLO contribution in χPT could already be substantial at the pion mass around 300–500 MeV. To really confirm the expected pion mass dependence in the NNLO fit, we need lattice data in the pion mass region of 200–250 MeV.

A similar analysis for the scalar form factor of the pion is also presented in [42]. For this quantity, the expected chiral logarithm is even stronger, and the comparison with χPT is very interesting. We calculated the scalar form factor using the all-to-all quark propagator technique, including the disconnected quark-loop diagram contributions. For details, see [42].

5.2. Kaon semileptonic form factor

Whether the strange quark can be treated within the SU(3) χPT is an important issue, since the main sources of phenomenological information for kaon physics rely on χPT. For instance, the

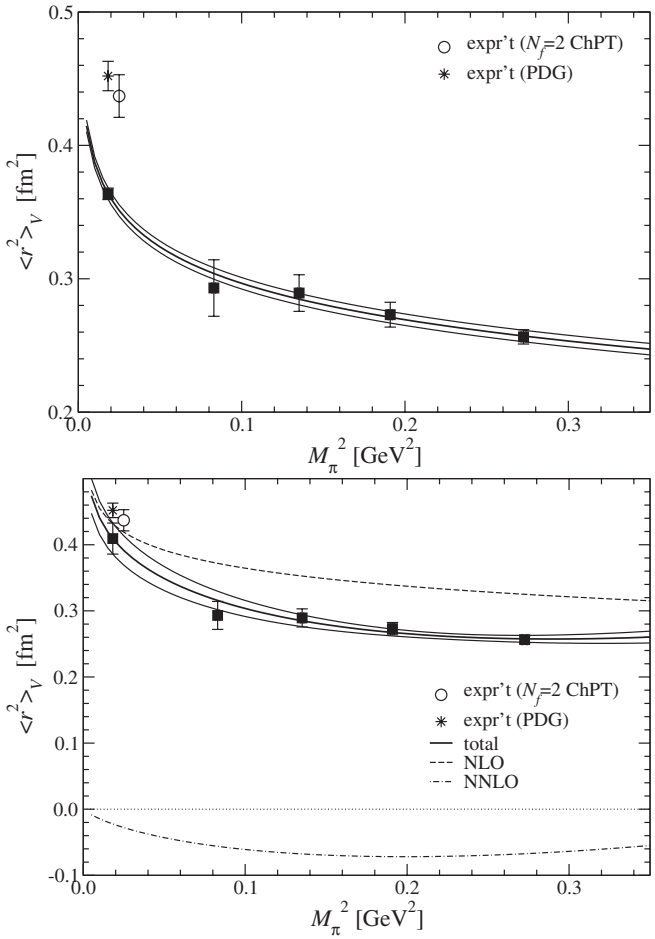

Fig. 8. Top: Pion charge radius and the χPT fit at NLO. Experimental data are shown by a star. Bottom: The same data are fitted with the NNLO formula. Individual contributions of NLO and NNLO are drawn with dashed and dash–dotted curves. Plots from [42].

determination of a Cabibbo–Kobayashi–Maskawa (CKM) matrix element $|V_{us}|$ uses the semileptonic decays $K \to \pi \ell \nu$. The determination of $|V_{us}|$ is very precise because the relevant form factor $f_+(q^2)$ is normalized to 1 at $q^2 = 0$ in the degenerate quark mass limit; deviation from this was estimated using the SU(3) χPT and some phenomenological models [62,63], which would eventually be replaced by lattice calculations. The lattice calculations still require information from χPT on the pion mass dependence in order to reliably perform chiral extrapolation, as in the case of the pion form factor.

The kaon semileptonic decay form factors $f_\pm(q^2)$ are defined through

$$\langle \pi(p')|V_\mu|K(p)\rangle = (p+p')_\mu f_+(q^2) + (p-p')_\mu f_-(q^2), \tag{5.3}$$

with $q_\mu = (p-p')_\mu$. Here, V_μ is a $\Delta S = 1$ vector current. One also defines a scalar form factor $f_0(q^2) = f_+(q^2) + f_-(q^2) \times q^2/(m_K^2 - m_\pi^2)$. In the limit of vanishing q^2, $f_+(0) = f_0(0)$. Unlike the pion form factor, $f_+(0)$ is not exactly normalized to be unity, but its small difference from one, which is of order $(m_s - m)^2$, is of major interest in the determination of $|V_{us}|$.

Lattice calculation of $f_\pm(q^2)$ can be done in a similar manner to the pion form factor, except that one has to disentangle $f_+(q^2)$ and $f_-(q^2)$ using different polarizations of V_μ. The results at $m_\pi \simeq 540$ MeV are shown in Fig. 9. Both $f_+(q^2)$ and $f_0(q^2)$ are nearly normalized to 1 at $q^2 = 0$

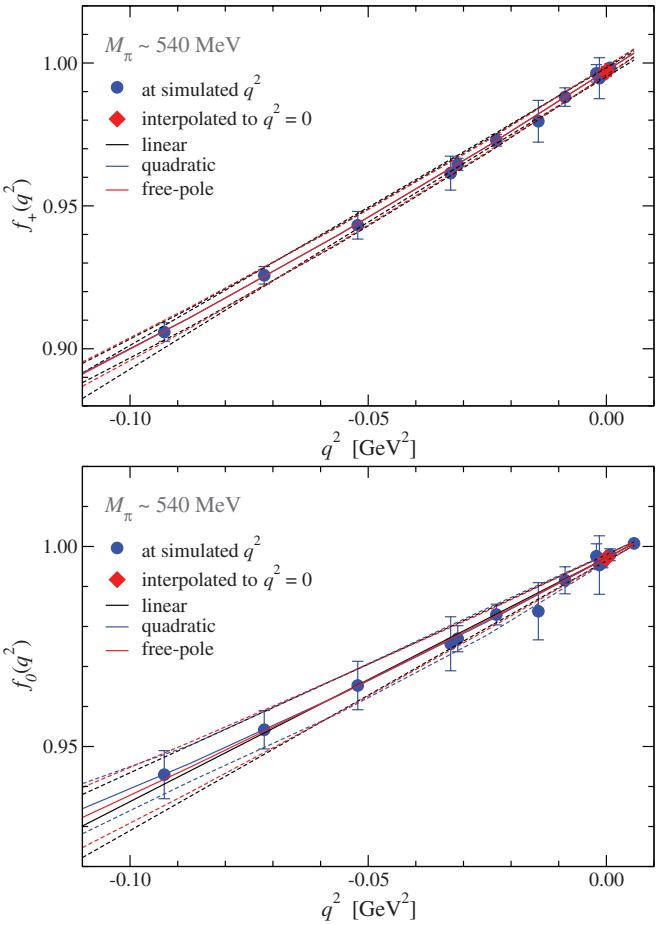

Fig. 9. Kaon semileptonic form factors $f_+(q^2)$ (top) and $f_0(q^2)$ (bottom) from a calculation on the $2+1$-flavor lattice configurations. The pion mass in this plot is relatively heavy ($m_\pi \sim 540$ MeV).

and the slope in q^2 is precisely determined. Compared to the plot for the pion decay constant (Fig. 7), the q^2 range is very close to $q^2 = 0$. This is possible because we are using the twisted boundary condition technique [64], which enables us to assign momenta that are not multiples of $2\pi/L$. We use it on top of the all-to-all propagator method.

For the form factor $f_+(q^2)$ we may define the radius parameter $\langle r^2 \rangle_V^{K\pi}$, which is an analog of the pion charge radius. Chiral extrapolation of $\langle r^2 \rangle_V^{K\pi}$ is shown in Fig. 10 (top). According to χPT, the divergence in the chiral limit is not as strong as that for the pion form factor, and our extrapolation using an NLO formula is consistent with the experimental value. The shape of the other form factor $f_-(q^2)$ (or $f_0(q^2)$) can be parameterized by $\xi(q^2) \equiv f_-(q^2)/f_+(q^2)$, which is roughly a constant in q^2. A chiral extrapolation of $\xi(0)$ is shown in Fig. 10 (bottom) as a function of $m_K^2 - m_\pi^2$. (Note that $\xi(q^2)$ vanishes in the limit of degenerate m_K and m_π.) Again, the result is consistent with the experimental value. This preliminary analysis [65] will be further refined and presented elsewhere, including the result for the most important quantity, i.e. $f_+(0)$.

5.3. Neutral kaon mixing

The kaon bag parameter B_K, defined by

$$B_K(\mu) = \frac{\langle \bar{K}^0 | \bar{d}\gamma_\mu(1-\gamma_5)s\, \bar{d}\gamma_\mu(1-\gamma_5)s | K^0 \rangle}{\frac{8}{3} f_K^2 m_K^2}, \tag{5.4}$$

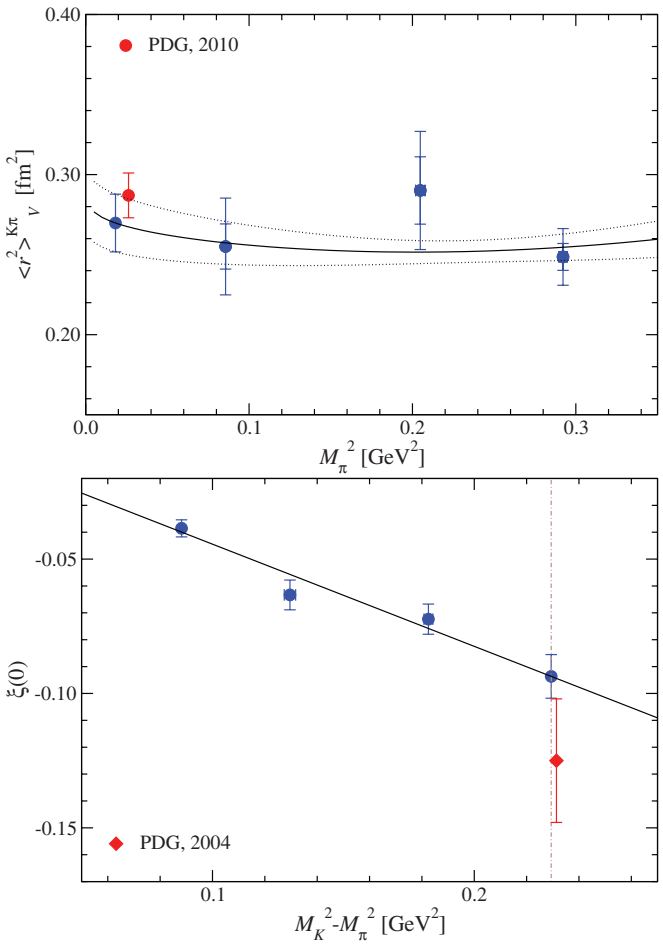

Fig. 10. Top: chiral extrapolation of the radius $\langle r^2\rangle_V^{K\pi}$. Bottom: a form factor ratio $\xi(q^2) \equiv f_-(q^2)/f_+(q^2)$ at $q^2 = 0$. Extrapolation to the physical point of $m_K^2 - m_\pi^2$, indicated by a vertical dashed line, is shown.

affects the strength of the indirect CP violation in neutral kaon mixing, from which one can put a constraint on the Cabibbo–Kobayashi–Maskawa (CKM) matrix elements, and its precise calculation is of direct relevance to the physics of quark flavor mixings. Lattice calculation of B_K reaps the benefit of the exact chiral symmetry of the overlap fermion, because the relevant four-quark operator

$$O_{LL} = \bar{d}\gamma_\mu(1-\gamma_5)s\,\bar{d}\gamma_\mu(1-\gamma_5)s \tag{5.5}$$

may mix with operators of other chiral structures when the chiral symmetry is explicitly violated on the lattice. With the overlap fermion, there is no such problem and the renormalization factor that relates the lattice operator to its continuum counterpart is simply multiplicative. Its calculation can be done non-perturbatively using the RI/MOM scheme as an intermediate renormalization scheme [66].

Besides this operator mixing problem, the calculation method for B_K is now rather standard. One takes a ratio of the relevant three-point function $\langle P_{\bar{s}u}\,O_{LL}\,P_{\bar{u}s}\rangle$ to a product of two-point functions corresponding to the denominator of (5.4), $\langle P_{\bar{s}u}\,A_0\rangle\langle A_0\,P_{\bar{u}s}\rangle$, where P are interpolating operators of the kaon (or antikaon) and A_0 is the axial-vector current of a flavor structure $\bar{s}u$ or $\bar{u}s$. From the ratio, one finds a plateau corresponding to the ground state contribution and extracts B_K from its amplitude. Our result in two-flavor QCD [67] is $B_K(2\,\mathrm{GeV}) = 0.537(4)(40)$ after extrapolating the lattice data to physical down and (valence) strange quark masses. The chiral extrapolation for B_K is very stable because the result turned out to depend only on $m_d + m_s$.

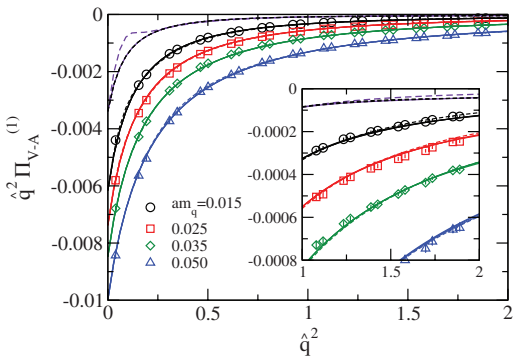

Fig. 11. Difference of the vacuum polarization function $q^2\Pi^{(1)}_{V-A}(q^2)$ calculated on the lattice at four different quark masses. Reproduced from [70].

We have also performed a calculation on our $2+1$-flavor gauge configurations and the result for B_K is essentially unchanged. According to a recent summary of various lattice results, an average $B_K(2\,\mathrm{GeV}) = 0.536(17)$ has been obtained [68].

5.4. *VV − AA correlator*

The vacuum polarization function $(\Pi_J)_{\mu\nu}(q^2) = (q^2\delta_{\mu\nu} - q_\mu q_\nu)\Pi^{(1)}_J(q^2)$ is a rich source of information on QCD dynamics. In particular, the difference between the vector and axial-vector current vacuum polarizations, $\Pi^{(1)}_{V-A}(q^2) = \Pi^{(1)}_V(q^2) - \Pi^{(1)}_A(q^2)$, is sensitive to the spontaneously broken chiral symmetry in the QCD vacuum. When the vacuum is chirally symmetric, $\Pi^{(1)}_{V-A}(q^2)$ must vanish in the massless limit, while it may develop a pion-pole $-f_\pi^2/q^2$ near $q^2 = 0$, when spontaneous chiral symmetry breaking occurs. A slope of $q^2\Pi^{(1)}_{V-A}(q^2)$ at $q^2 = 0$ corresponds to L_{10}, one of the LECs at one-loop χPT. Even more interesting is its relation to the mass difference between neutral and charged pions. Namely, in the massless limit of up and down quarks, there is a relation obtained using current algebra techniques [69]:

$$m^2_{\pi^\pm} = -\frac{3\alpha}{4\pi}\int_0^\infty dq^2 \frac{q^2\Pi^{(1)}_{V-A}(q^2)}{f^2}, \tag{5.6}$$

where α represents the fine structure constant and f is the pion decay constant in the massless limit.

In order to calculate the difference $\Pi^{(1)}_{V-A}(q^2)$ on the lattice with any useful precision, the exact chiral symmetry realized by the overlap fermion plays a crucial role. We notice that each of $\Pi^{(1)}_J(q^2)$ ($J = V$ or A) is logarithmically divergent while their difference must vanish in the absence of chiral symmetry breaking. This means that the cancellation in the difference $\Pi^{(1)}_V(q^2) - \Pi^{(1)}_A(q^2)$ is uncontrollable unless keeping chiral symmetry very precisely on the lattice.

On our two-flavor gauge configurations we calculate the vacuum polarization functions $\Pi^{(1)}_J(q^2)$ and in particular their difference $\Pi^{(1)}_{V-A}(q^2)$ [70]. Figure 11 shows the results in the form $q^2\Pi^{(1)}_{V-A}(q^2)$ obtained at four different quark masses (shown by different symbols: triangle, diamond, square, and circle from heavier to lighter). As anticipated, this quantity becomes smaller (in magnitude) as the quark mass is decreased, but there is a left-over even in the chiral limit (thick red curve). (A dashed curve shows another chiral extrapolation attempt, including chiral logarithms.) Its residue at $q^2 = 0$ corresponds to f^2 and its integral over the entire q^2 range gives $m^2_{\pi^\pm} - m^2_{\pi^0}$. Our result is $m^2_{\pi^\pm} = 993(12)(^{+0}_{-135})(149)\,\mathrm{MeV}^2$ in the chiral limit.

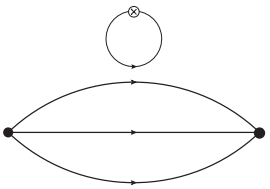

Fig. 12. Disconnected three-point function appearing in the calculation of $\langle N|\bar{s}s|N\rangle$. Lines show quark propagators dressed by virtual gluons and sea quarks. The three connected lines represent the nucleon propagation and the disconnected loop arises from the strange scalar operator $\bar{s}s$ shown by a cross symbol.

In the context of composite Higgs boson models, where a QCD-like theory is assumed to form bound states, the relevant LEC, i.e. L_{10}, corresponds to Peskin–Takeuchi's S-parameter [71] and $m^2_{\pi^\pm}$ corresponds to the mass of the pseudo-Nambu–Goldstone boson. Therefore, also in this direction, our work opens up a new possibility for the calculation of interesting physical quantities.

5.5. Nucleon sigma term and strange quark content

Using lattice QCD, one can address questions on nucleon structure. One interesting question is what the nucleon mass m_N is made of. Nucleon may have a mass m_0 even in the massless limit of up and down quarks; the extra amount due to finite quark masses is called the nucleon sigma term $\sigma_{\pi N}$, so that $m_N = m_0 + \sigma_{\pi N}$. The sigma term can be written in terms of a matrix element as

$$\sigma_{\pi N} = m_{ud}\langle N|\bar{u}u + \bar{d}d|N\rangle, \tag{5.7}$$

where m_{ud} denotes the (degenerate) up and down quark mass. In the definition of $\langle N|\bar{u}u + \bar{d}d|N\rangle$, a subtraction of the vacuum contribution $V\langle 0|\bar{u}u + \bar{d}d|0\rangle$ is understood. Furthermore, there might be a contribution from the strange quark in the sea, $m_s\langle N|\bar{s}s|N\rangle$, which is called the strange quark content of the nucleon. A common parameterization is the y parameter:

$$y \equiv \frac{2\langle N|\bar{s}s|N\rangle}{\langle N|\bar{u}u + \bar{d}d|N\rangle}. \tag{5.8}$$

Phenomenological estimates of y have been quite limited in the past and its lattice calculation is of great help. Recently, there has been renewed interest in this quantity, as it may greatly influence the cross section of some dark matter candidates to hit ordinary matter (see, for instance, [72]).

Lattice calculation of these quantities may be performed through two different strategies. One possibility is to directly calculate the matrix elements $\langle N|\bar{u}u + \bar{d}d|N\rangle$ and $\langle N|\bar{s}s|N\rangle$ from the relevant three-point functions. The other method is to calculate a derivative of m_N in terms of m_{ud} and m_s; using the Feynman–Hellman theorem these are related to the matrix elements in (5.7) and (5.8).

Let us start the discussion with the second method. On the lattice there is freedom to take the valence quark mass different from sea quark mass. We may calculate the nucleon mass at various values of sea and valence quarks. Then, by a global fit using the formula motivated by the chiral effective theory, the derivatives in terms of m_{ud} and m_s are obtained. In this way we obtain $\sigma_{\pi N} = 52(2)(^{+20}_{-7})(^{+5}_{-0})$ MeV and $y = 0.030(16)(^{+6}_{-8})(^{+1}_{-2})$ in two-flavor QCD [73]. The former is in the same ball-park as phenomenological analysis, while the result for y is an order of magnitude smaller than the values from previous lattice calculations such as [74].

The small value of y is confirmed by an independent calculation using the first method, i.e. a direct calculation of the matrix elements. The direct lattice calculation of the strange quark content is nontrivial because it requires a calculation of a disconnected quark-loop diagram depicted in Fig. 12.

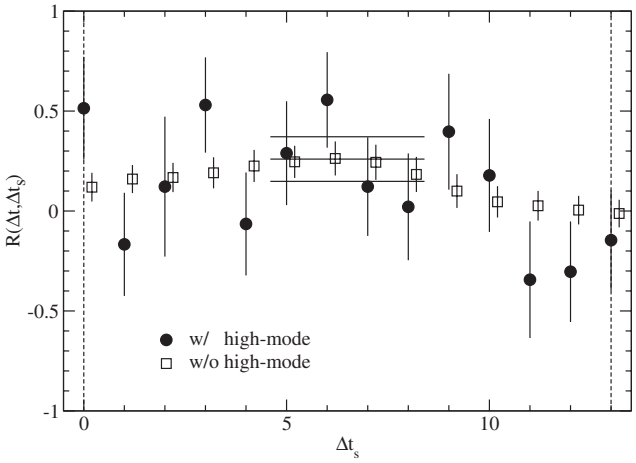

Fig. 13. Three-point function relevant to $\langle N|\bar{s}s|N\rangle$ divided by a two-point nucleon correlation function. Open symbols show the data with the low-mode contribution only for the disconnected quark-loop; filled symbols include high modes. Reproduced from [75].

One must sum over the location of the strange scalar operator $\bar{s}s$, which is too costly without using a dedicated method such as the all-to-all quark propagator technique. We use this method as discussed in Sect. 3.4.

An example of the lattice data [75] is shown in Fig. 13. Here we plot the disconnected three-point function, from which we extract $\langle N|\bar{s}s|N\rangle$, divided by a two-point nucleon correlation function. Open symbols show the data for which only the low-mode contribution is included in the disconnected quark-loop; filled symbols include the rest of the fermion modes using the all-to-all quark propagator technique. A non-zero signal is obtained for the open symbols. The filled symbols including high modes are much noisier, but after performing a constant fit we obtain a statistically non-zero signal in the plateau region because the high-mode contribution is statistically independent among different points of Δt_s, the location of the $\bar{s}s$ operator. After chiral extrapolation we obtain $y = 0.050(12)(34)$ in two-flavor QCD, which supports the calculation through the Feynman–Hellman theorem and favors the small y parameter.

An extension of these calculations to $2+1$-flavor QCD is ongoing and preliminary results are already presented in [76,77].

5.6. $\pi^0 \to \gamma\gamma$ decay

The anomaly sector of quantum gauge theory is most dramatically reflected in the $\pi^0 \to \gamma\gamma$ process. Without the axial-anomaly (or the Adler–Bell–Jackiw (ABJ) anomaly [78]), its amplitude is highly suppressed compared to the experimental data. Once we take account of the axial-anomaly, the amplitude can be calculated very precisely since the one-loop calculation is known to give the result valid to all orders in the limit of vanishing pion mass [79]. Corrections due to finite quark mass are a non-perturbative problem, which we address in this subsection. If the calculation is precise enough, we may test the anomaly sector of quantum gauge theory beyond the leading order against the experimental data.

The $\pi^0 \to \gamma\gamma$ transition form factor $f_{\pi^0\gamma\gamma}(p_1, p_2)$ is defined through a matrix element of two electromagnetic currents V_μ

$$\int d^4x e^{ip_2x} \langle \pi^0(q)|V_\nu(x)V_\mu(0)|0\rangle = \epsilon_{\mu\nu\alpha\beta} p_1^\alpha p_2^\beta f_{\pi^0\gamma\gamma}(p_1, p_2), \tag{5.9}$$

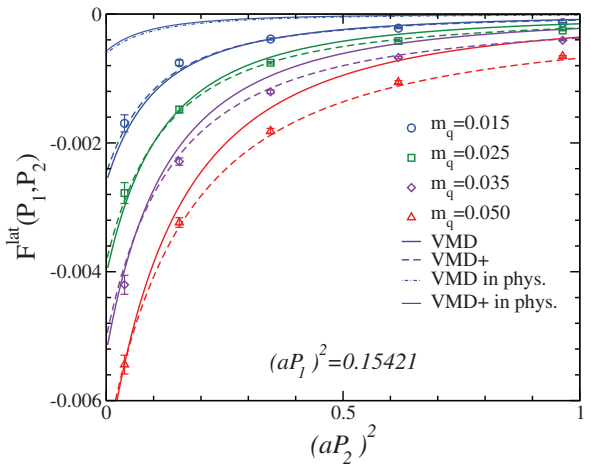

Fig. 14. A normalized $\pi^0 \to \gamma\gamma$ form factor $F^{\rm lat}(P_1, P_2)$ as a function of P_2^2. Data at a fixed P_1^2 are shown for four values of quark mass. Curves are fits with the vector dominance model (VMD) or VMD-motivated models. Reproduced from [80].

where p_1 and p_2 are photon momenta and $q_\mu = -(p_1 + p_2)_\mu$ is the pion four-momentum. The ABJ anomaly implies $f_{\pi^0\gamma\gamma}(0, 0) = 1/(4\pi^2 f)$ in the massless pion limit with f the pion decay constant in the massless limit. (In this section we use a normalization of $f \simeq 90$ MeV.) To perform the lattice calculation of $f_{\pi^0\gamma\gamma}(p_1, p_2)$ we replace the pion state in (5.9) in favor of the axial vector current or pseudoscalar density, and calculate a three-point function of the form $\langle 0|P(x)V_\nu(y)V_\mu(0)|0\rangle$. By a Fourier transformation for both x and y in four dimensions, we obtain the three-point function in momentum space, which should have a momentum dependence as

$$\int d^4x d^4y\, e^{-i(qx+p_1y)}\langle 0|2mP(x)V_\nu(y)V_\mu(0)|0\rangle$$
$$= -\frac{f_\pi m_\pi^2}{-q^2+m_\pi^2}\epsilon_{\mu\nu\alpha\beta}p_1^\alpha p_2^\beta f_{\pi^0\gamma\gamma}(p_1, p_2) + \cdots, \tag{5.10}$$

where the dominant pion-pole contribution is explicitly written while other contributions are represented by ellipses. Since the lattice is defined in the Euclidean space-time, the momentum available in this way is always space-like, i.e. q^2, $p_i^2 < 0$. Then, as far as we can neglect the higher resonance contributions, the calculation of $f_{\pi^0\gamma\gamma}(p_1, p_2)$ in the space-like region is straightforward.

Such a calculation is carried out in [80,81]. A fit of the lattice data for

$$F^{\rm lat}(P_1, P_2) = -\frac{f_\pi m_\pi^2}{Q^2+m_\pi^2} f_{\pi^0\gamma^*\gamma^*}(P_1, P_2) \tag{5.11}$$

is demonstrated in Fig. 14. (Here, $Q^2 = -q^2$ and $P_i^2 = -p_i^2$.) The fit assumes the vector meson dominance (VMD) model

$$F^{\rm VMD}(P_1, P_2) = -\frac{m_\pi^2}{Q^2+m_\pi^2} X_a G_V(P_1, m_V)G_V(P_2, m_V), \tag{5.12}$$

where $G_V(P, m_V)$ is a vector meson propagator $G_V(P, m_V) = m_V^2/(P^2 + m_V^2)$. The parameter X_a is an overall constant that must be $1/(4\pi^2) = 0.02533$ if the ABJ anomaly is realized in the massless limit. Our result, obtained by fitting the lowest momentum points (the leftmost symbols in the plot), is 0.0260(6) and is consistent with the expectation. At higher momenta we find a deviation from the VMD model, especially for larger quark masses. We therefore attempt to extend the model to include

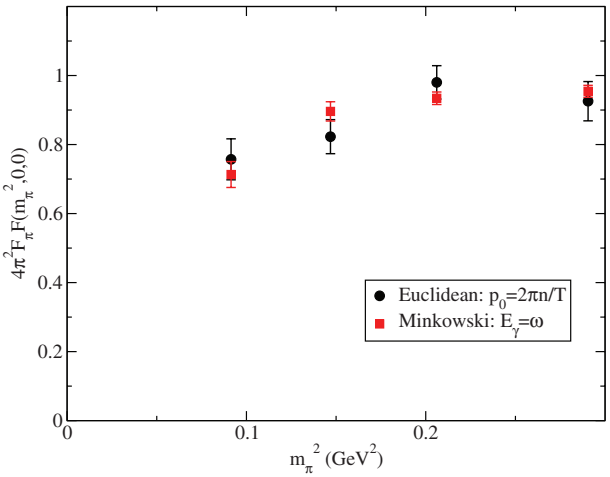

Fig. 15. Normalized on-shell form factor of the $\pi^0 \to \gamma\gamma$ decay. Results are shown for both the Euclidean and Minkowski methods. Reproduced from [85].

higher resonance contributions. An attempt to fit the data using the χPT predictions at one-loop is presented in [81].

More recently, we applied a method to extract the lowest-lying π^0 state while inserting nearly arbitrary four-momenta for final photons [82–84], combined with the all-to-all quark propagator technique [85] (for a similar attempt, but without all-to-all, see [86]). On $2+1$-flavor configurations we calculate the $\pi^0 \to \gamma\gamma$ form factor and confirm that the result agrees with the analysis of the Euclidean momenta as shown in Fig. 15. The plot also shows a significant deviation from the ABJ anomaly, $F(m_\pi^2, 0, 0) = 1/(4\pi^2 f)$ in the chiral limit. This is likely due to the finite volume effect, for which further studies are ongoing, including a calculation of a large-volume lattice.

Another motivation for this study is to use the form factor for off-shell photons in order to estimate the hadronic light-by-light scattering ($\gamma^*\gamma^* \to \gamma^*\gamma^*$) amplitude, which is necessary in the precise calculation of the muon anomalous magnetic moment $g-2$. Because the pion is light, the virtual process $\gamma^*\gamma^* \to \pi^0 \to \gamma^*\gamma^*$ would give the dominant contribution. The lattice calculation may provide an input for such analysis.

6. Physics applications at higher energy scales

The overlap fermion formulation is most powerful when studying the low-energy dynamics of QCD where chiral symmetry plays a special role. However, in this section we focus on an observable for which the dynamics at higher energy scales is important. Namely, we analyze the vacuum polarization function $\Pi_J(Q^2)$ at high Q^2 to determine the strong coupling constant α_s and other quantities.

6.1. Strong coupling constant

Since the strong coupling constant "runs" under the change of the scale of interest, lattice determination of the strong coupling constant is equivalent to a setting of the lattice scale $1/a$ at a given bare coupling constant $\alpha_s^{\rm lat}$. Once we establish the relation $\alpha_s^{\rm lat}(a^{-1})$, we may also convert the relation to more familiar definitions, such as the one in the $\overline{\rm MS}$ scheme, using perturbation theory as $\alpha_s^{\overline{\rm MS}}(\mu) = Z(\mu a)\alpha_s^{\rm lat}(a^{-1})$. Therefore, precise determination of α_s requires good control of systematic errors in the perturbative matching factor $Z(\mu a)$. This is the reason that the previous lattice

calculation by the HPQCD collaboration [87,88] employed an automated perturbation method to calculate very complicated two-loop contributions on the lattice.

In our work, we develop a method to use the vacuum polarization function $\Pi_V(Q^2)$ at short distances. In particular, we consider the Adler function [89]:

$$D(Q^2) \equiv -Q^2 \frac{d\Pi_V(Q^2)}{dQ^2}, \tag{6.1}$$

which is a physical quantity related to the e^+e^- annihilation cross section. Since this quantity does not have an ultraviolet divergence, the perturbative calculation in the continuum theory obtained with dimensional regularization can be directly applied for the lattice data. This means that one may fit the lattice data using the known continuum perturbative formula to three-loop order (or even four-loop for the leading term) supplemented by an operator product expansion (OPE) in $1/Q^2$. The fit parameters are then $\alpha_s^{\overline{\rm MS}}(\mu)$ as well as a few coefficients of OPE. In this way we may bypass the complicated lattice perturbation theory and take advantage of using the well developed continuum perturbation theory.

To be more explicit, we write down the OPE formula for $\Pi_{V+A}(Q^2) = \Pi_V(Q^2) + \Pi_A(Q^2)$:

$$\Pi_{V+A}(Q^2) = c + C_0(Q^2, \mu^2, \alpha_s) + C_m(Q^2, \mu^2, \alpha_s)\frac{m^2(Q^2)}{Q^2} + \sum_{q=u,d,s} C_{\bar{q}q}(Q^2, \alpha_s)\frac{\langle m_q \bar{q}q\rangle}{Q^4} + C_{GG}(Q^2, \alpha_s)\frac{\langle (\alpha_s/\pi)GG\rangle}{Q^4} + O(1/Q^6). \tag{6.2}$$

The first term c is a scheme-dependent constant, which is divergent. In physical quantities, such as the Adler function, this term does not contribute. The coefficients in the second term, which is the leading contribution, are perturbatively calculated to four-loop order in the $\overline{\rm MS}$ scheme [92], and other perturbative functions are also known to high enough orders. At the order of $1/Q^4$ of OPE, vacuum expectation values of operators $m_q\bar{q}q$ and $(\alpha_s/\pi)G^2_{\mu\nu}$ are involved. In our work, the chiral condensate $\langle\bar{q}q\rangle$ is calculated from other methods and here it is just an input parameter. The other parameter $\langle(\alpha/\pi)G^2_{\mu\nu}\rangle$ is sometimes called the gluon condensate. Lattice calculation of this quantity is not feasible because the operator $G^2_{\mu\nu}$ mixes with the identity operator. Subtraction of the identity operator requires an extremely precise determination of the mixing coefficient since it is strongly divergent ($\sim 1/a^4$). In this work we simply treat $\langle(\alpha/\pi)G^2_{\mu\nu}\rangle$ as a fit parameter and determine it from the Q^2 dependence of $\Pi_{V+A}(Q^2)$. (We do not quote the numerical result for $\langle(\alpha/\pi)G^2_{\mu\nu}\rangle$, because the relation to the "gluon condensate" in some phenomenological papers is not known.)

Using this method, we extract α_s for two-flavor [90] and $2+1$-flavor QCD [91]. The vacuum polarization function $\Pi_{V+A}(Q^2)$ is calculated at values of space-like Q^2 below $(aQ)^2 < 1$. The discretization effect is not substantial in this range of $(aQ)^2$, which is confirmed by looking at different momentum definitions equivalent up to $O(a^2)$ effects and by carrying out a perturbative calculation for the overlap fermion to estimate the size of deviation from the continuum theory. An example of the fits of (6.2) to the lattice data in $2+1$-flavor QCD is shown in Fig. 16. Data at four different quark masses in the range $0.4 < (aQ)^2 < 1.0$ are well fitted by (6.2) with only three free parameters, i.e. $\alpha_s^{\overline{\rm MS}}(\mu)$, $\langle(\alpha_s/\pi)GG\rangle$, and c. The stability of the fitted value against the fit range is carefully checked. Indeed, the $1/Q^6$ corrections are visible below $(aQ)^2 < 0.4$.

Our result in $2+1$-flavor QCD, $\alpha_s^{(5)}(M_Z) = 0.1181(3)(^{+14}_{-12})$ [91], is consistent with the previous best lattice calculation [87,88], which gave $\alpha_s^{(5)}(M_Z) = 0.1183(8)$. The size of the error is also comparable.

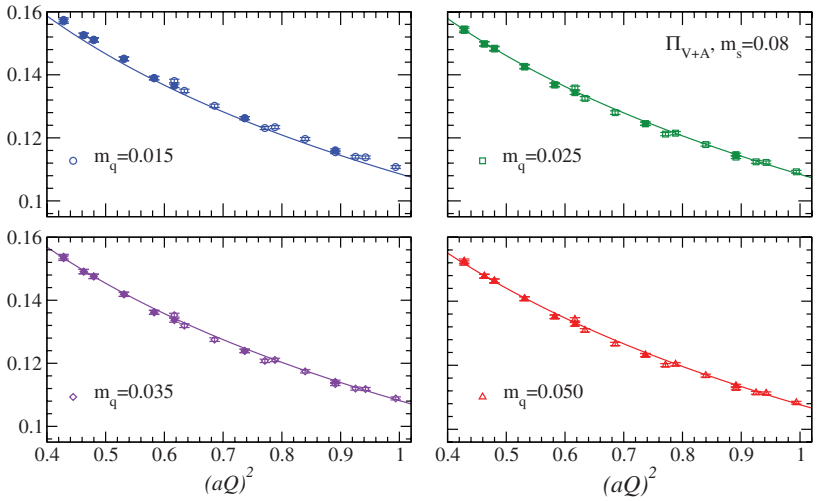

Fig. 16. Fit of the vacuum polarization function on the lattice with continuum perturbative calculation. Four panels show the data at different quark masses; all the data are fitted simultaneously. Plots from [91].

A closely related method has been developed by the HPQCD collaboration, which used the charmonium two-point function. By taking an appropriate moment in the coordinate space, the ultraviolet divergence is removed and the lattice data can be directly fitted with a corresponding continuum calculation, as in our work using the vacuum polarization function with light quarks. The result is $\alpha_s(M_Z) = 0.1174(12)$ [93]. With this method, one can also determine the charm quark mass at the same time.

7. Finite-temperature QCD

The finite-temperature phase transition of QCD, which is expected to occur in the early universe and in heavy-ion collision experiments, is considered to be a chiral phase transition—the order parameter is $\langle \bar{q}q \rangle$. Therefore, its lattice simulation is desired to be performed using the formulation preserving chiral symmetry. This is the reason that the staggered fermion has been used in most of the previous finite-temperature lattice QCD simulations. Besides the famous problem of "rooting" [94], the staggered fermion has a delicate problem of flavor (or *taste* in recent terminology) violation. At finite lattice spacing, the Nambu–Goldstone (NG) pion of the exact chiral symmetry of the staggered fermion is only one of 15 pions. Other non-NG pions are typically 300–500 MeV heavier than the NG pion. There is a potential problem that the physics of the phase transition occurring at the transition temperature around 180 MeV may be distorted by such a mismatch of the particle content. A simulation using the overlap fermion formulation provides a theoretically clean approach to this problem. Given the numerical cost required for the overlap fermion, it will be important work to be performed on next-generation supercomputers.

In this section, we describe an early such attempt that focuses on the restoration of the axial $U(1)$ symmetry.

7.1. Restoration of the axial $U(1)$ symmetry

The role of the axial anomaly of QCD in the finite-temperature transition is a slightly confusing problem. There is literature [95] that argues that the axial $U(1)$ symmetry is restored, together with

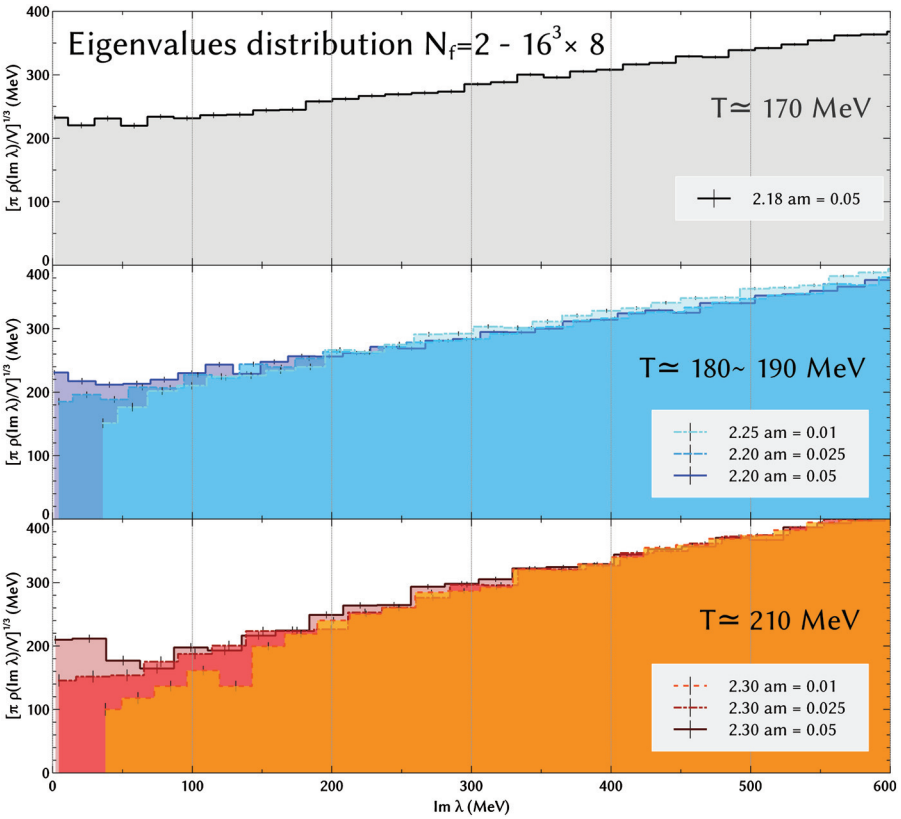

Fig. 17. Spectral density $\rho(\lambda)$ of the overlap-Dirac operator at finite temperature. Near the transition temperature (∼180 MeV), we observe a decrease of $\rho(0)$ as the quark mass is decreased. At quark masses lower than, say, 30 MeV, the spectral density shows a gap at zero. Reproduced from [97].

the flavor non-singlet $SU(2)$ chiral symmetry, at the phase transition point, but this sounds peculiar, because the axial $U(1)$ symmetry is violated by a quantum effect even at short distances.

There is a possibility that axial $U(1)$ is effectively restored in the particle spectrum above the phase transition. Namely, all the particles that form a multiplet under $U(2) \times U(2)$ become degenerate. In the (pseudo)scalar sector, they are π, η, σ, and δ (or a_0). Indeed, if there is no near-zero mode accumulation of the Dirac operator, this could happen as discussed in [95].

We carried out a series of dynamical overlap fermion simulations at finite temperature on a $16^3 \times 8$ lattice [96,97]. Two degenerate quark flavors are included with mass in a range $m_s/5$–m_s. The global topological charge is fixed to zero as in our work at zero temperature. This may induce finite volume effects, but we numerically confirm in the quenched theory at finite temperature that we are able to reproduce topological susceptibility on these lattices using the method outlined in Sect. 4.3.

Figure 17 shows the spectral density $\rho(\lambda)$ of the overlap-Dirac operator at temperatures in the range 170–210 MeV, which presumably sandwiches the transition temperature. We observe that $\rho(0)$ stays finite even above the phase transition when the quark mass is heavy (∼100 MeV). As the quark mass is decreased, the spectral function vanishes above the phase transition (∼180 MeV). Indeed, we find a spectral gap at zero in the high-temperature phase.

On these lattices we calculated the (pseudo)scalar meson correlators and found that the correlators coincide among π, η, σ, and δ [97]. This means that the contribution from the disconnected quark-loop diagram vanishes. This is observed when there is a gap in the spectral function. Our result indicates that the axial $U(1)$ symmetry is effectively restored in the high-temperature phase of QCD.

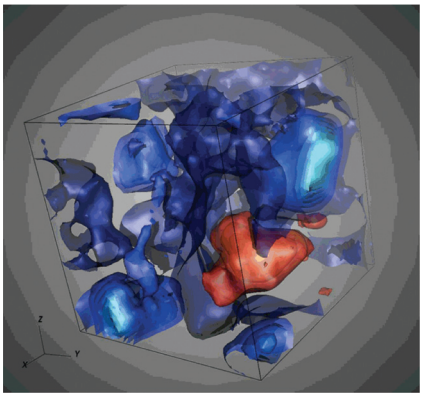

Fig. 18. A snapshot of the QCD vacuum calculated on a dynamical overlap configuration. The lattice size is $24^3 \times 48$ and the light quark mass is at the lightest available value ($am = 0.015$), which corresponds to a pion mass around 290 MeV. Red and blue regions distinguish positive and negative chirality ($\bar{u}_1(x)\gamma_5 u_1(x)$) of the lowest-lying (but non-zero) eigenmode $u_1(x)$.

8. Summary and perspective

Lattice simulation of QCD has matured to the level that one can reproduce the experimental results for the simplest physical quantities, such as low-lying hadron masses. This is a result of a number of theoretical and technical ideas accumulated over the last 30 years, as well as of the exponential growth of computational power. It is only in the last few years that the major lattice QCD groups have been able to simulate QCD including up, down, and strange quarks with their masses reasonably close to their physical values.

One important goal of lattice QCD is, of course, to give precise calculations that can be used to test the Standard Model of elementary particles. Another motivation for performing its simulation is to push the understanding of the dynamics of QCD into a deeper level. The work performed by the JLQCD and TWQCD collaborations is in this direction. Since spontaneous breaking of chiral symmetry plays a central role in forming the QCD vacuum, we employed the overlap fermion formulation that preserves exact chiral symmetry even at finite lattice spacings. This beautiful property allows us to study the profile of the QCD vacuum through the spectral density of the Dirac operator, for instance. Through this quantity we find the accumulation of low-lying fermion modes, as anticipated by the Banks–Casher relation.

We could gain further insight into the property of the QCD vacuum. Figure 18 demonstrates a spatial distribution of the lowest-lying Dirac eigenmode. Different colors represent left-handed and right-handed chirality components. We observe that the low modes are spatially localized and chirally polarized, which supports a picture that drove researchers to instanton-based models (see, for instance, [98]), although more precise quantitative tests are needed to further confirm or refute those particular models.

There are many other physics applications of our simulations, as discussed in this article. For many of them, the exact chiral symmetry is beneficial to simplifying theoretical analysis or even crucial to extract meaningful signals. The all-to-all quark propagator technique that we extensively applied has also proven to be very useful. Through this work, we have greatly extended the horizons of lattice QCD calculations.

On the other hand, it is obvious that realizing chiral symmetry on the lattice requires a substantial extra computational cost compared to other standard lattice fermion formulations, such as Wilson

or staggered fermions. This sets a severe limitation on the lattice spacing and lattice volume we can reach with the overlap fermion. In order to achieve more precise calculations at small lattice spacings, the development of a new theoretical formulation and/or simulation scheme, in which the numerical simulation is substantially faster but where good chiral symmetry is maintained, is necessary. Work is in progress in this direction.

Acknowledgements

We thank the members of the JLQCD and TWQCD collaborations for numerous discussions. Numerical simulations were performed on the Hitachi SR11000 and IBM System Blue Gene Solution at the High Energy Accelerator Research Organization (KEK) with the support of its Large Scale Simulation Program (Nos. 06-13, 07-16, 08-05, 09-05, 09/10-09, and 10-11). This work is supported in part by a Grant-in-aid for Scientific Research of Japan (Nos. 18340075, 20105001, 20105002, 20105005, 21674002, 23105710, 23105714). and by the Taiwan National Science Council (Nos. NSC99-2112-M-002-012-MY3, NSC99-2112-M-001-014-MY3) and NTU-CQSE (No. 10R80914-4).

References

[1] K. G. Wilson, Phys. Rev. D **10**, 2445 (1974).
[2] Y. Iwasaki [CP-PACS Collaboration], Nucl. Phys. Proc. Suppl. **60A**, 246 (1998).
[3] Y. Iwasaki, Prog. Theor. Phys. Suppl. **138**, 1 (2000).
[4] E. E. Scholz, PoS **LAT2009**, 005 (2009).
[5] S. Weinberg, Physica A **96**, 327 (1979).
[6] J. Gasser and H. Leutwyler, Ann. Phys. **158**, 142 (1984).
[7] H. B. Nielsen and M. Ninomiya, Nucl. Phys. B **185**, 20 (1981).
[8] H. B. Nielsen and M. Ninomiya, Nucl. Phys. B **193**, 173 (1981).
[9] D. B. Kaplan, Phys. Lett. B **288**, 342 (1992).
[10] Y. Shamir, Nucl. Phys. B **406**, 90 (1993).
[11] V. Furman and Y. Shamir, Nucl. Phys. B **439**, 54 (1995).
[12] H. Neuberger, Phys. Lett. B **417**, 141 (1998).
[13] H. Neuberger, Phys. Lett. B **427**, 353 (1998).
[14] M. Luscher, Phys. Lett. B **428**, 342 (1998).
[15] T. Banks and A. Casher, Nucl. Phys. B **169**, 103 (1980).
[16] P. H. Ginsparg and K. G. Wilson, Phys. Rev. D **25**, 2649 (1982).
[17] P. Hasenfratz, V. Laliena, and F. Niedermayer, Phys. Lett. B **427**, 125 (1998).
[18] S. Duane, A. D. Kennedy, B. J. Pendleton, and D. Roweth, Phys. Lett. B **195**, 216 (1987).
[19] B. Alles, G. Boyd, M. D'Elia, A. Di Giacomo, and E. Vicari, Phys. Lett. B **389**, 107 (1996).
[20] L. Del Debbio, G. M. Manca, and E. Vicari, Phys. Lett. B **594**, 315 (2004).
[21] Z. Fodor, S. D. Katz, and K. K. Szabo, J. High Energy Phys. **0408**, 003 (2004).
[22] T. A. DeGrand and S. Schaefer, Phys. Rev. D **71**, 034507 (2005).
[23] S. Aoki, H. Fukaya, S. Hashimoto, and T. Onogi, Phys. Rev. D **76**, 054508 (2007).
[24] R. Brower, S. Chandrasekharan, J. W. Negele, and U. J. Wiese, Phys. Lett. B **560**, 64 (2003).
[25] C. Vafa and E. Witten, Phys. Rev. Lett. **53**, 535 (1984).
[26] S. Aoki and H. Fukaya, Phys. Rev. D **81**, 034022 (2010).
[27] S. Aoki *et al.* [JLQCD Collaboration], Phys. Rev. D **78**, 014508 (2008).
[28] H. Matsufuru *et al.* [JLQCD Collaboration], PoS LAT **2006**, 031 (2006).
[29] H. Matsufuru *et al.* [JLQCD and TWQCD Collaborations], PoS LATTICE **2008**, 077 (2008).
[30] N. Cundy, J. van den Eshof, A. Frommer, S. Krieg, T. Lippert, and K. Schafer, Comput. Phys. Commun. **165**, 221 (2005).
[31] A. Borici, arXiv:hep-lat/9912040.
[32] R. Narayanan and H. Neuberger, Phys. Rev. D **62**, 074504 (2000).
[33] A. Borici, arXiv:hep-lat/0402035.
[34] R. G. Edwards, B. Joo, A. D. Kennedy, K. Orginos, and U. Wenger, PoS **LAT2005**, 146 (2006).
[35] P. Hernandez, K. Jansen, and M. Luscher, Nucl. Phys. B **552**, 363 (1999).
[36] S. Aoki and Y. Taniguchi, Phys. Rev. D **65**, 074502 (2002).

[37] M. Golterman, Y. Shamir, and B. Svetitsky, Phys. Rev. D **71**, 071502 (2005).
[38] M. Golterman, Y. Shamir, and B. Svetitsky, Phys. Rev. D **72**, 034501 (2005).
[39] N. Yamada *et al.* [JLQCD Collaboration], PoS **LAT2006**, 060 (2006).
[40] H. Fukaya, S. Hashimoto, K. I. Ishikawa, T. Kaneko, H. Matsufuru, T. Onogi, and N. Yamada [JLQCD Collaboration], Phys. Rev. D **74**, 094505 (2006).
[41] J. Foley, K. J. Juge, A. O'Cais, M. Peardon, S. M. Ryan, and J. I. Skullerud, Comput. Phys. Commun. **172**, 145 (2005).
[42] S. Aoki *et al.* [JLQCD and TWQCD Collaborations], Phys. Rev. D **80**, 034508 (2009).
[43] P. H. Damgaard and H. Fukaya, J. High Energy Phys. **0901**, 052 (2009).
[44] H. Fukaya, S. Aoki, S. Hashimoto, T. Kaneko, J. Noaki, T. Onogi, and N. Yamada [JLQCD Collaboration], Phys. Rev. Lett. **104**, 122002 (2010).
[45] H. Fukaya, S. Aoki, S. Hashimoto, T. Kaneko, J. Noaki, T. Onogi, and N. Yamada [JLQCD Collaboration], Phys. Rev. Lett. **105**, 159901 (2010) [erratum].
[46] H. Fukaya *et al.* [JLQCD and TWQCD Collaborations], Phys. Rev. D **83**, 074501 (2011).
[47] H. Fukaya *et al.* [JLQCD Collaboration], Phys. Rev. Lett. **98**, 172001 (2007).
[48] H. Fukaya *et al.*, Phys. Rev. D **76**, 054503 (2007).
[49] J. Noaki, T. W. Chiu, H. Fukaya, S. Hashimoto, H. Matsufuru, T. Onogi, E. Shintani, and N. Yamada, Phys. Rev. D **81**, 034502 (2010).
[50] H. Fukaya *et al.* [JLQCD Collaboration], Phys. Rev. D **77**, 074503 (2008).
[51] S. Aoki and H. Fukaya, Phys. Rev. D **84**, 014501 (2011).
[52] H. Fukaya *et al.* [JLQCD Collaboration], arXiv:1111.0417 [hep-lat].
[53] H. Leutwyler and A. V. Smilga, Phys. Rev. D **46**, 5607 (1992).
[54] S. Aoki *et al.* [JLQCD and TWQCD Collaborations], Phys. Lett. B **665**, 294 (2008).
[55] T. W. Chiu *et al.* [JLQCD and TWQCD Collaborations], PoS **LAT2008**, 072 (2008).
[56] T. H. Hsieh *et al.* [JLQCD and TWQCD Collaborations], PoS LAT **2009**, 085 (2009).
[57] C. Bernard, S. Hashimoto, D. B. Leinweber, P. Lepage, E. Pallante, S. R. Sharpe, and H. Wittig, Nucl. Phys. Proc. Suppl. **119**, 170 (2003).
[58] J. Noaki *et al.* [JLQCD and TWQCD Collaborations], Phys. Rev. Lett. **101**, 202004 (2008).
[59] J. Noaki *et al.*, PoS **LATTICE2008**, 107 (2008).
[60] J. Noaki *et al.* [TWQCD and JLQCD Collaborations], PoS **LAT2009**, 096 (2009).
[61] J. Noaki *et al.* [JLQCD and TWQCD Collaborations], PoS **LATTICE2010**, 117 (2010).
[62] J. Gasser and H. Leutwyler, Nucl. Phys. B **250**, 517 (1985).
[63] H. Leutwyler and M. Roos, Z. Phys. C **25**, 91 (1984).
[64] P. F. Bedaque, Phys. Lett. B **593**, 82 (2004).
[65] T. Kaneko *et al.* [JLQCD Collaboration], PoS **LATTICE2011**, 284 (2011).
[66] G. Martinelli, C. Pittori, C. T. Sachrajda, M. Testa, and A. Vladikas, Nucl. Phys. B **445**, 81 (1995).
[67] S. Aoki *et al.* [JLQCD Collaboration], Phys. Rev. D **77**, 094503 (2008).
[68] G. Colangelo *et al.*, Eur. Phys. J. C **71**, 1695 (2011).
[69] T. Das, G. S. Guralnik, V. S. Mathur, F. E. Low, and J. E. Young, Phys. Rev. Lett. **18**, 759 (1967).
[70] E. Shintani *et al.* [JLQCD Collaboration], Phys. Rev. Lett. **101**, 242001 (2008).
[71] M. E. Peskin and T. Takeuchi, Phys. Rev. Lett. **65**, 964 (1990).
[72] J. R. Ellis, K. A. Olive, and C. Savage, Phys. Rev. D **77**, 065026 (2008).
[73] H. Ohki *et al.*, Phys. Rev. D **78**, 054502 (2008).
[74] S. Gusken *et al.* [TXL Collaboration], Phys. Rev. D **59**, 054504 (1999).
[75] K. Takeda, S. Aoki, S. Hashimoto, T. Kaneko, J. Noaki, and T. Onogi [JLQCD Collaboration], Phys. Rev. D **83**, 114506 (2011).
[76] K. Takeda, S. Aoki, S. Hashimoto, T. Kaneko, T. Onogi, and N. Yamada [JLQCD Collaboration], PoS **LATTICE2010**, 160 (2010).
[77] T. Kaneko [for the JLQCD Collaboration], PoS **ICHEP2010**, 368 (2010).
[78] S. L. Adler, Phys. Rev. **177**, 2426 (1969).
[79] S. L. Adler and W. A. Bardeen, Phys. Rev. **182**, 1517 (1969).
[80] E. Shintani, S. Aoki, S. Hashimoto, T. Onogi, and N. Yamada [JLQCD Collaboration], PoS **LAT2009**, 246 (2009).
[81] E. Shintani, S. Aoki, S. Hashimoto, T. Onogi, and N. Yamada, PoS **LATTICE2010**, 159 (2010).
[82] X. d. Ji and C. w. Jung, Phys. Rev. Lett. **86**, 208 (2001).
[83] X. d. Ji and C. w. Jung, Phys. Rev. D **64**, 034506 (2001).

[84] J. J. Dudek and R. G. Edwards, Phys. Rev. Lett. **97**, 172001 (2006).
[85] X. Feng *et al.*, PoS **LATTICE2011**, 154 (2011).
[86] S. D. Cohen, H. W. Lin, J. Dudek, and R. G. Edwards, PoS **LATTICE2008**, 159 (2008).
[87] Q. Mason *et al.* [HPQCD and UKQCD Collaborations], Phys. Rev. Lett. **95**, 052002 (2005).
[88] C. T. H. Davies, K. Hornbostel, I. D. Kendall, G. P. Lepage, C. McNeile, J. Shigemitsu, and H. Trottier [HPQCD Collaboration], Phys. Rev. D **78**, 114507 (2008).
[89] S. L. Adler, Phys. Rev. D **10**, 3714 (1974).
[90] E. Shintani *et al.* [JLQCD and TWQCD Collaborations], Phys. Rev. D **79**, 074510 (2009).
[91] E. Shintani, S. Aoki, H. Fukaya, S. Hashimoto, T. Kaneko, T. Onogi, and N. Yamada, Phys. Rev. D **82**, 074505 (2010).
[92] K. G. Chetyrkin and A. Maier, Nucl. Phys. B **844**, 266 (2011).
[93] I. Allison *et al.* [HPQCD Collaboration], Phys. Rev. D **78**, 054513 (2008).
[94] S. R. Sharpe, PoS **LAT2006**, 022 (2006).
[95] T. D. Cohen, Phys. Rev. D **54**, 1867 (1996).
[96] G. Cossu, S. Aoki, S. Hashimoto, T. Kaneko, H. Matsufuru, J. i. Noaki, and E. Shintani [JLQCD Collaboration], PoS **LATTICE2010**, 174 (2010).
[97] G. Cossu *et al.*, PoS **LATTICE2011**, 188 (2011).
[98] E. V. Shuryak and T. Schafer, Annu. Rev. Nucl. Part. Sci. **47**, 359 (1997).